

# Water Resources Research®

## RESEARCH ARTICLE

10.1029/2024WR039519

### Special Collection:

Drones for sensing freshwater ecosystems

### Key Points:

- A multi-elevation and -frequency UAV-GPR method is proposed to map soil permittivity and conductivity at the field (and larger) scale
- Unlike other published approaches, the proposed method is relatively simple and does not rely on full-waveform inversion
- The proposed method enhances permittivity estimation by accounting for the effects of conductivity

### Supporting Information:

Supporting Information may be found in the online version of this article.

### Correspondence to:

Q. Cheng,  
Qinbo.Cheng@hhu.edu.cn




### Citation:

Cheng, Q., Cheng, Y., Ma, Z., Binley, A., Liu, J., Zhang, Z., et al. (2025). Combined measurement of soil permittivity and electrical conductivity using UAV-based ground penetrating radar. *Water Resources Research*, 61, e2024WR039519. <https://doi.org/10.1029/2024WR039519>

Received 22 NOV 2024

Accepted 4 SEP 2025

## Combined Measurement of Soil Permittivity and Electrical Conductivity Using UAV-Based Ground Penetrating Radar

Qinbo Cheng<sup>1</sup> , Yu Cheng<sup>1</sup>, Zhijin Ma<sup>2</sup>, Andrew Binley<sup>3</sup> , Jintao Liu<sup>1,4</sup> , Zhicai Zhang<sup>1</sup>, Feng Huang<sup>1</sup>, and Xi Chen<sup>5</sup>

<sup>1</sup>College of Hydrology and Water Resources, Hohai University, Nanjing, China, <sup>2</sup>Yellow River Institute of Hydrology and Water Resources, Zhengzhou, China, <sup>3</sup>Lancaster Environment Centre, Lancaster University, Lancaster, UK, <sup>4</sup>National Key Laboratory of Water Disaster Prevention, Hohai University, Nanjing, China, <sup>5</sup>School of Earth System Science, Tianjin University, Tianjin, China

**Abstract** Measurements of soil water content and salinity are important for a wide range of topics, in particular those concerned with soil and plant health, and specific aspects of agricultural management. However, most traditional methods are unsuitable for simultaneously mapping the field scale variability of soil electrical properties. In this study, we propose a method that uses an unmanned aerial vehicle (UAV) to support ground penetrating radar (GPR) antennae with different frequencies, allowing spatial scanning of surface reflection coefficients, which is then used to estimate the soil relative permittivity ( $\epsilon_r$ ) and electrical conductivity ( $\sigma$ ). These parameters are then used to estimate soil water content and salinity using empirical transfer functions. Unlike other published approaches, the proposed method is relatively simple and does not rely on full-waveform inversion. Field tests in the riparian zone of the Yangtze River and salinized land close to the Yellow Sea are used to demonstrate the effectiveness of the method. The surveys illustrate that the UAV-GPR give results comparable to those measured in situ with a soil electrical property meter. These findings are supported by accuracy analysis using Monte Carlo simulation which reveal that the measurement error of  $\epsilon_r$  increases with  $\sigma$ , and the relative errors in  $\sigma$  measurements are generally less than those of  $\epsilon_r$  except in areas of high  $\epsilon_r$  and low  $\sigma$ . The study provides an approach for mapping soil electrical properties using UAV technology, thus opening up the possibility of remote sensing of spatial variability of these important properties at high spatial resolution.

**Plain Language Summary** Soil water content and salinity are critical for agricultural productivity, ecosystem health, and sustainable land management. Traditional methods for measuring these properties, such as lab-based soil sampling or ground sensors, are labor-intensive, spatially limited, or disruptive. Remote sensing offers broader coverage but struggles to balance resolution, cost, and accuracy. This study introduces a novel unmanned aerial vehicle (UAV) based system carrying ground-penetrating radar (GPR) with multi-frequency antennas to non-invasively map soil electrical properties (relative permittivity and electrical conductivity), which are empirically linked to water content and salinity. Unlike complex inversion-based approaches, this method uses surface reflection coefficients from GPR scans, enabling rapid, high-resolution field-scale surveys. Field tests in China's Yangtze River riparian zone and Yellow Sea salinized areas demonstrated strong agreement between UAV-GPR estimates and in situ soil sensor data. The approach avoids soil disturbance and costly fieldwork, addressing gaps in scalable, precise soil monitoring. By enabling detailed spatial mapping of soil variability, this UAV-GPR method supports precision agriculture (e.g., irrigation optimization), soil health assessment, and salinization management. It bridges the resolution gap between localized sensors and coarse satellite data, offering a practical tool for advancing hydrological research and sustainable land-use practices.

## 1. Introduction

Soil water content is critical for the support of terrestrial vegetation and other soil biota, and directly affects various hydrological processes such as evapotranspiration and infiltration (Babaeian et al., 2019; Brocca et al., 2017; Seneviratne et al., 2010). Soil salinity is an important index for evaluating land degradation and soil health (Butcher et al., 2016; Srivastava et al., 2019). Too low or too high soil water content and salinity values can both bring detrimental effects on plants. Therefore, the acquisition of soil water content and salinity information is important for understanding how to minimize plant stress and soil health degradation, in addition to providing

© 2025. The Author(s).

This is an open access article under the terms of the [Creative Commons Attribution-NonCommercial-NoDerivs License](#), which permits use and distribution in any medium, provided the original work is properly cited, the use is non-commercial and no modifications or adaptations are made.

data for effective irrigation and fertilization management of cultivated farmland, sustainable agricultural practice and ecosystem conservation (Shamshiri et al., 2022).

Traditionally, the measurement of soil water content and salinity is conducted using a range of direct and indirect methods. Direct methods, which includes gravimetric analysis for measuring soil water content and vacuum pumping for soil water sampling to assess salinity, typically involves extracting samples in the field and measuring soil characteristic parameters in the laboratory (Brocca et al., 2017; Rhoades, 1993; Susha Lekshmi et al., 2014). Although direct measurements are often regarded as more reliable than other methods, they have a relatively small measurement support volume, which necessitates substantial labor costs for mapping the spatial variability of soil properties and states. Furthermore, direct methods are destructive, which may constrain their use in a number of applications.

Indirect methods measure a different soil electrical property (e.g., relative permittivity ( $\epsilon_r$ , dimensionless) and electrical conductivity ( $\sigma$ )), which are then used in conjunction with an appropriate functional relationship to estimate soil moisture and salinity. Such methods can be implemented through ground-based, proximal, and satellite remote sensing platforms (Babaeian et al., 2019; Corwin, 2008; Mane et al., 2024; Rhoades, 1993). Many ground-based methods, such as the time-domain reflectometry (TDR) for soil  $\epsilon_r$  and  $\sigma$ , are generally invasive and inefficient for assessing variation at a large scale. At a contrasting scale, the relatively new ground-based cosmic-ray sensing method can provide integrated estimates of soil moisture over relatively large areas (Andreasen et al., 2017). Remote sensing technologies provide effective tools for regional surveys of ground soil moisture and salinity (Metternicht & Zinck, 2003; Petropoulos et al., 2015). However, the remote sensing community faces a trade-off among data quality, spatial coverage, acquisition costs, and high accuracy (Turner, 2014).

In practice, there is often a need to assess the in-field spatial variability of soil properties and states, particularly for agricultural management. This intermediate scale may be examined using a number of geophysical methods, such as ground penetrating radar (GPR), electrical resistivity tomography (ERT) and electromagnetic induction (EMI). These methods provide reasonably large measurement support volume and are typically non- or minimally invasive. Ground-based mobile (e.g., proximal) platforms have been developed for a number of these methods or variants. Recent rapid development of unmanned aerial vehicle (UAV) technology provides a valuable airborne platform for a broad application of a number of geophysical methods, particularly as UAVs are widely accessible, inherently mobile, safe and affordable (Acharya et al., 2021; Lopez et al., 2022; Velez-Nicolas et al., 2021). The UAV-based geophysical technologies have an important advantage over earlier methods by not requiring the operator ground access to the survey area, thus avoiding disturbance and land degradation, which could be important in sensitive or protected areas (Cheng et al., 2023).

In recent years, several UAV-based instruments have been developed to investigate the spatial distribution of soil  $\epsilon_r$  and  $\sigma$ . For example, based on the full-waveform inversion method for soil water content mapping, Wu et al. (2019) proposed a UAV-GPR equipped with a lightweight hybrid horn-dipole antenna, while Dehem (2020) developed another UAV-GPR with a monostatic dipole antenna. They further proposed a UAV-GPR with a monostatic dipole antenna to combinedly measure the  $\epsilon_r$  and  $\sigma$  (Dehem, 2020; Lambot et al., 2006; Wu et al., 2019; Wu & Lambot, 2022). However, the full-waveform approach involves relatively complex processing steps, such as antenna calibration and geophysical inversion. Furthermore, its measurement accuracy depends on the estimation of the antenna transfer functions and the electronic stability of the radar system (Lambot et al., 2004).

Cheng et al. (2023) proposed a more simple and effective method to estimate the soil water content without the need for bespoke antennae. The method employs widely available shielded radar antennas mounted on a UAV to measure the surface reflection coefficient, enabling the calculation of soil  $\epsilon_r$ . However, the method proposed by Cheng et al. (2023) does not take into account the effect of soil EC on the surface reflection coefficient, which could lead to errors in soils with high  $\sigma$  (Brovelli & Cassiani, 2011; Robinson et al., 2003; Wilson et al., 2024; Wu & Lambot, 2022). Many studies have pointed out that the effect of  $\sigma$  on reflection coefficient increases as GPR frequency decreases (Tulaczyk & Foley, 2020; Ward & Hohmann, 1988; Wu & Lambot, 2022). Our aim here is to improve the UAV-based shielded GPR method by combining the measurement of  $\epsilon_r$  and  $\sigma$ .

In this study, we propose a method to measure the surface reflection coefficient values for different frequency antennas, and then according to the measured values, employ an appropriate optimization algorithm to estimate the soil  $\epsilon_r$  and  $\sigma$ . Following this, soil water content and salinity can be estimated using empirical transfer functions

(Hilhorst, 2000; Topp et al., 1980). We test the method at two field sites (a riparian zone and a salinized farmland) and compare the measurements with those determined from a conventional in-field sensor. Finally, before offering some overall conclusions, we analyze the accuracy and the influence factors of the UAV-GPR method, including: the investigation depth, surface roughness, and surface slope.

## 2. Methodology

### 2.1. Relationship Between Reflection Coefficient and Soil Permittivity and Conductivity

The normal-incidence reflection coefficient ( $\xi$ ) at a planar interface between two media is defined as the ratio of the amplitudes of the reflected and incident plane waves:

$$\xi = \frac{A_{\text{ref}}}{A_{\text{in}}}, \quad (1)$$

where  $A_{\text{ref}}$  and  $A_{\text{in}}$  are, respectively, the amplitude of reflected and incident waves.

In the frequency domain, the (plane-wave) reflection coefficient ( $\psi$ ) of ground surface can be written (when incidence is normal) (Slob & Fokkema, 2002) as:

$$\psi = \frac{\sqrt{\omega^2 \mu_0 \epsilon_0} - \sqrt{\omega^2 \mu \epsilon_0 \epsilon_r - j\omega \mu \sigma}}{\sqrt{\omega^2 \mu_0 \epsilon_0} + \sqrt{\omega^2 \mu \epsilon_0 \epsilon_r - j\omega \mu \sigma}}, \quad (2)$$

where  $\omega$  is the angular frequency ( $=2\pi f$ ,  $f$  is the frequency of electromagnetic (EM) wave, Hz);  $\mu_0$  and  $\mu$  are, respectively, the magnetic permeability of free space ( $=4\pi \times 10^{-7}$  H/m) and of the soil layer;  $\epsilon_0$  is the dielectric permittivity of free space ( $=8.85 \times 10^{-12}$  F/m);  $\epsilon_r$  is the relative permittivity of soil layer (dimensionless);  $\sigma$  is the electrical conductivity of soil layer (S/m), that is, the bulk electrical conductivity; and  $j$  is an imaginary unit.

For most soils,  $\mu$  generally equals  $\mu_0$  (Scott, 1983), thus, Equation 2 can be simplified to:

$$\psi = \frac{1 - \sqrt{\epsilon_r - j\sigma/\omega\epsilon_0}}{1 + \sqrt{\epsilon_r - j\sigma/\omega\epsilon_0}}, \quad (3)$$

where  $\sigma/\omega\epsilon_0$  is usually treated as the imaginary part of relative permittivity.

The above equation shows that if we can use different frequency antennas to measure the surface soil reflection coefficient, we can state simultaneous equations for  $\epsilon_r$  and  $\sigma$  under the assumption that  $\epsilon_r$  and  $\sigma$  do not change with the electromagnetic frequency:

$$\begin{cases} \psi_1 = \frac{1 - \sqrt{\epsilon_r - j\sigma/\omega_1\epsilon_0}}{1 + \sqrt{\epsilon_r - j\sigma/\omega_1\epsilon_0}} \\ \psi_2 = \frac{1 - \sqrt{\epsilon_r - j\sigma/\omega_2\epsilon_0}}{1 + \sqrt{\epsilon_r - j\sigma/\omega_2\epsilon_0}} \\ \vdots \\ \psi_i = \frac{1 - \sqrt{\epsilon_r - j\sigma/\omega_i\epsilon_0}}{1 + \sqrt{\epsilon_r - j\sigma/\omega_i\epsilon_0}} \\ \vdots \\ \psi_n = \frac{1 - \sqrt{\epsilon_r - j\sigma/\omega_n\epsilon_0}}{1 + \sqrt{\epsilon_r - j\sigma/\omega_n\epsilon_0}} \end{cases}, \quad (4)$$

where  $\omega_1, \omega_2, \omega_i, \omega_n$  are the angular frequencies used for measurements;  $\psi_1, \psi_2, \psi_i$ , and  $\psi_n$  are the corresponding surface reflection coefficients at those frequencies.

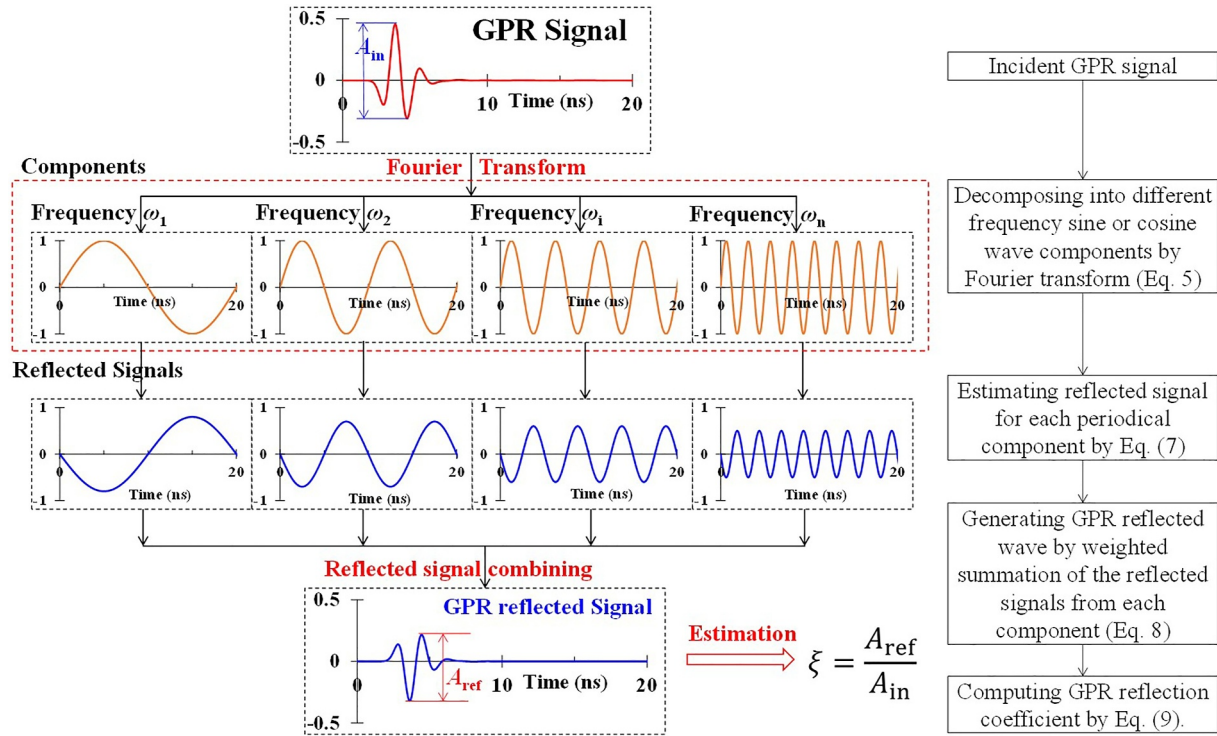


**Figure 1.** A flow chart for estimation of GPR reflection coefficient using the Fourier transform method.

The values of  $\epsilon_r$  and  $\sigma$  can be determined using the least squares method based on the simultaneous Equation 4. Since there are only two unknown parameters ( $\epsilon_r$  and  $\sigma$ ) in Equation 4, in practice, only two different frequency antennas are needed to measure the soil reflection coefficient and further estimate the  $\epsilon_r$  and the  $\sigma$ . However, Wu and Lambot (2022) found that the sensitivity of  $\psi$  to  $\sigma$  and  $\epsilon_r$  varies with frequency. High-frequency radar waves are less sensitive to  $\sigma$ , while low-frequency radar waves are less sensitive to  $\epsilon_r$ . Therefore, to avoid ill-posedness in Equation 4, it is recommended that a combination of high- and low-frequency radar are used.

## 2.2. Simulation and Measurement Methods of Soil Reflection Coefficient for GPR

As commonly used pulse GPR waves belong to the family of time domain signals, it is not possible to use Equation 3 directly to estimate the reflection coefficient. However, by applying the Fourier transform, the incident GPR signal can be decomposed into sine and cosine waves of different frequencies as shown in Figure 1:

$$f(t) = \frac{1}{2\pi} \int_{-\infty}^{\infty} F(\omega) e^{j\omega t} d\omega, \quad (5)$$

where  $f(t)$  represents the time-varying pulse-GPR signal,  $F(\omega)$  denotes the complex amplitude coefficient corresponding to the frequency component  $e^{j\omega t}$ , which can be estimated via the Fourier transform:

$$F(\omega) = \int_{-\infty}^{\infty} f(t) e^{-j\omega t} dt, \quad (6)$$

For discrete pulse-GPR signals, the Fast Fourier Transform (FFT) can be used to estimate  $F(\omega)$ . These decomposed sine and cosine components can then be applied in Equation 3 to estimate the reflection coefficient as a function of frequency, enabling the simulation of the corresponding reflected wave ( $R(\omega)$ ) of  $e^{j\omega t}$  (Figure 1):

$$R(\omega) = \psi e^{j\omega t} = \frac{1 - \sqrt{\epsilon_r - j\sigma/\omega\epsilon_0}}{1 + \sqrt{\epsilon_r - j\sigma/\omega\epsilon_0}} e^{j\omega t}, \quad (7)$$

By synthesizing the reflected waves of different-frequency sine/cosine components obtained from the Fourier transform, the GPR reflected signal ( $f'(t)$ ) is generated as follows:

$$f'(t) = \frac{1}{2\pi} \int_{-\infty}^{\infty} F(\omega) R(\omega) d\omega = \frac{1}{2\pi} \int_{-\infty}^{\infty} F(\omega) \psi e^{j\omega t} d\omega, \quad (8)$$

The reflection coefficient of the incident GPR wave can be directly estimated from the amplitude ratio of the incident wave to its reflected counterpart (Equation 1):

$$\xi = \frac{A_{\text{ref}}}{A_{\text{in}}} = \frac{\max(f'(t)) - \min(f'(t))}{\max(f(t)) - \min(f(t))}. \quad (9)$$

A detailed flowchart for estimating the reflection coefficient of GPR signals is presented in Figure 1. This figure illustrates the simulation of the normal-incidence reflected GPR signal using the Fourier transform method. The proposed method replaces the use of Equation 3 with Equation 1 to theoretically calculate the surface soil reflection coefficient for GPR applications. However, this method carries an implicit assumption that, over the limited frequency band (such as 100–250 MHz), the dielectric properties can be approximated as constant—a common simplification in GPR literature when the relative change is small, for example, in dry or saturated sands (Lambot et al., 2005; Tran et al., 2012; Tran et al., 2014; Wu & Lambot, 2022). Future extensions could employ a Debye or Cole–Cole dispersion model to more accurately retrieve frequency-dependent dielectric parameters.

The incident GPR signal shown in Figure 1 can be acquired via an electromagnetic sensor. For convenience, it may also be estimated from the direct-wave signal recorded by the GPR receiving antenna. Although some studies have suggested that the antenna's direct-wave signal is prone to near-field interference and therefore may not accurately represent the far-field incident GPR signal depicted in Figure 1 (Tran et al., 2014), numerical simulation results indicate that surface reflection coefficient estimates based on this direct-wave signal closely match theoretical values (see Supporting Information S1).

Figure 1 demonstrates the theoretical method for calculating the surface reflection coefficient using pulse-GPR. For field measurements, this study employs the multi-elevation air-launched GPR method proposed by Cheng et al. (2023) to measure the surface reflection coefficient. They demonstrated that for the shielded bow-tie antenna, the product of the GPR height and the ratio of the surface-reflected wave amplitude to the direct-wave amplitude is proportional to the ground surface reflection coefficient, with the proportionality constant defined as the GPR shape factor ( $k$ ). Furthermore, Cheng et al. (2023) noted that using multi-elevation measurements can reduce GPR observational errors. This methodology involves the following computation:

$$\xi = \frac{1}{n} \left( \frac{1}{k} \sum_{i=1}^n \frac{A}{A_0} \right) H_i, \quad (10)$$

where  $n$  denotes the number of repeated measurements at different antenna heights;  $k$ , referred to as the GPR shape factor, is an empirical coefficient dependent on antenna characteristics such as the Tx-Rx separation distance, antenna directivity, and antenna geometry, and can be calibrated using survey results over materials with known surface reflection coefficients, for example, a metallic plate or a freshwater surface;  $A$  and  $A_0$  are, respectively, the amplitudes of reflected and direct (air) waves recorded by the GPR receiving antenna;  $i$  is the index for each measurement;  $H_i$  is the GPR antenna height for the  $i$ th measurement, calculated from the travel-time difference between the first extrema of the direct and reflected waves recorded by the GPR receiving antenna.

The multi-elevation method is based on the assumption of a homogeneous subsurface, and therefore it does not account for the footprint effect. Field measurements indicate that the footprint has little impact on ground-surface reflection-coefficient measurements, as demonstrated by Cheng et al. (2023). A possible reason is that the central area of the footprint contributes more to the measured reflection coefficient than the surrounding regions.

### 2.3. Principle of UAV-GPR to Simultaneously Measure Permittivity and Conductivity

Cheng et al. (2023) pointed out that Equation 10 is appropriate for most shielded antennas, as their directional radiation patterns reduce interference from lateral wave and UAV. However, for unshielded antennas with broader radiation patterns, the presence of strong lateral waves or UAV EM interferences may introduce additional measurement uncertainties, making this approach less effective. For the retrieval of  $\epsilon_r$  and  $\sigma$ , we can use different frequency antennas to measure the surface soil reflection coefficient, and further use these reflection coefficients to build the simultaneous equations (similar to Equation 4):

$$\begin{cases} \xi_1 = Re_{GPR1}(\epsilon_r, \sigma) \\ \xi_2 = Re_{GPR2}(\epsilon_r, \sigma) \\ \vdots \\ \xi_i = Re_{GPRi}(\epsilon_r, \sigma) \\ \vdots \\ \xi_n = Re_{GPRn}(\epsilon_r, \sigma) \end{cases}, \quad (11)$$

where  $\xi_1, \xi_2, \xi_i, \xi_n$  are the normal-incidence reflection coefficients measured by the multi-elevation air-launched GPR method proposed by Cheng et al. (2023);  $Re_{GPR1}, Re_{GPR2}, Re_{GPRi}$ , and  $Re_{GPRn}$  are the corresponding surface reflection coefficients theoretically calculated from Figure 1 for different frequency GPRs.

Similar to the simultaneous Equation 4, the least squares method is used to solve the simultaneous Equation 11 for estimation of  $\epsilon_r$  and  $\sigma$ . A detailed flow chart is presented in Figure 2.

Based on the estimated  $\epsilon_r$  value, the soil water content ( $\theta$ ) can be estimated by following, for example, the empirical equation for mineral soils (Topp et al., 1980):

$$\theta = -5.3 \times 10^{-2} + 2.92 \times 10^{-2} \epsilon_r - 5.5 \times 10^{-4} \epsilon_r^2 + 4.3 \times 10^{-6} \epsilon_r^3. \quad (12)$$

Based on the estimated  $\epsilon_r$  and  $\sigma$  values, the pore water electrical conductivity ( $\sigma_w$ ) can be estimated by following, for example, Hilhorst (2000):

$$\sigma_w = \frac{\epsilon_p \sigma}{\epsilon_r - C_0}, \quad (13)$$

where  $\epsilon_p$  is the relative permittivity of pore water ( $\approx 80$ );  $C_0$  is a parameter, which is equivalent to the permittivity at which the bulk electrical conductivity is zero ( $\approx 3.4$  for most inorganic soils) (Hilhorst, 2000).

$\sigma_w$  and  $\theta$  can be used to estimate soil salinity by the empirical relationship between electrical conductivity, soil water content and soil salinity, which can be derived from laboratory measurements (Corwin & Yemoto, 2019; Mu et al., 2024):

$$M = a \times \sigma_w \theta + b, \quad (14)$$

where  $M$  is the soil salinity (g/kg);  $a$  is the conversion coefficient between the salinity of the soil leaching solution and its electrical conductivity;  $b$  is the salinity in soil solid; both  $a$  and  $b$  are constants determined in the laboratory.

In this study, soil water content, pore-water electrical conductivity, and salinity are estimated using the empirical Equations 12–14 based on our measured permittivity and electrical conductivity, which inherently introduces some uncertainty. In particular, salinity estimates may suffer compounded errors because they depend on the prior estimates of both water content and pore-water conductivity. Therefore, for applications requiring higher accuracy, we recommend collecting local soil samples to recalibrate the relevant empirical relationships.

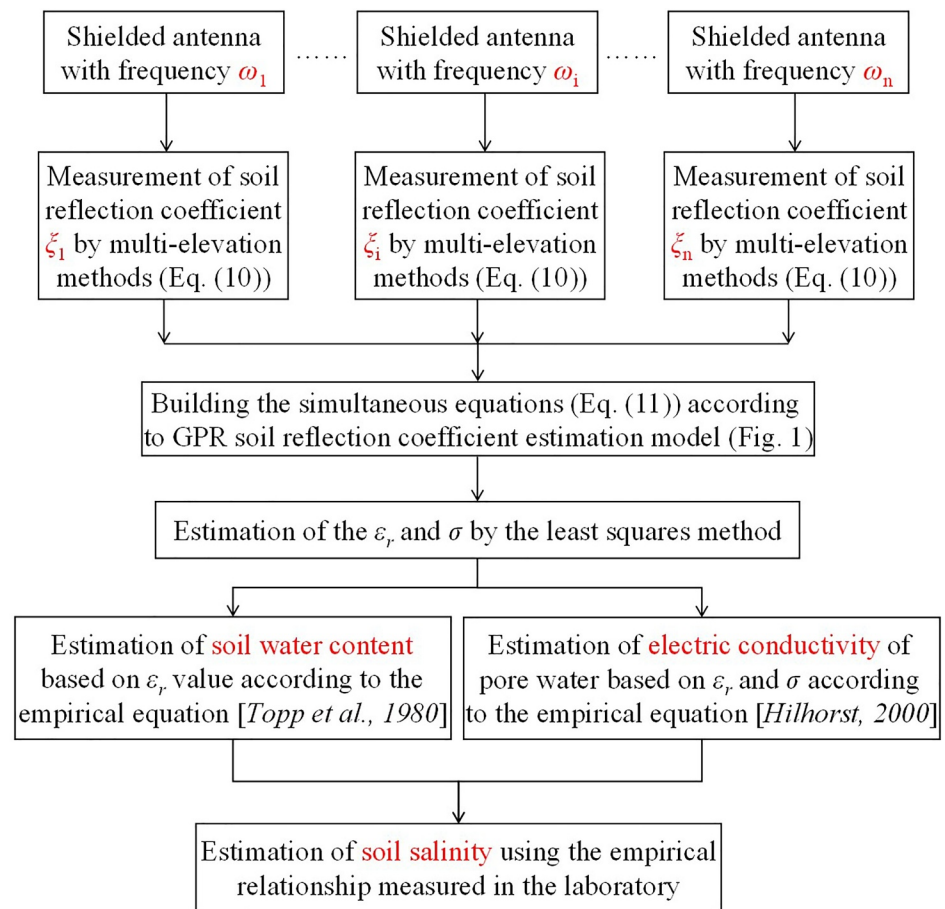


**Figure 2.** A flow chart for estimation of soil water content and salinity by UAV-GPR.

### 3. Field Test

In order to apply the approach for measuring soil  $\epsilon_r$  and  $\sigma$ , a 7.85 kg 250 MHz and a 25.5 kg 100 MHz shielded antenna from Mala® were selected and separately suspended from a DJI® T30 UAV by two ropes each with 2.0 m in length as shown in Figure 3. Because of the shielded antenna used, the EM interference from the UAV on the GPR's measurement of ground-reflected waves can be neglected. The GPR control unit was also attached on the UAV (Figure 3), and employed a time-triggered measurement method. The DJI® T30 UAV used was chosen because of its high-accuracy positioning system, a maximum loading capacity of 30 kg, and a user-friendly operating system interface, which allows the operator to plan the flight route and survey height for autonomous flight. It is also conducive to the multi-elevation measurements of our UAV-GPR approach.

As it is difficult to communicate between the UAV and GPR system, a Real-Time Kinematic positioning technique (RTK) system (S86, of which the horizontal and vertical positional accuracies are, respectively,  $\pm 0.01$  and  $\pm 0.03$  m) from South Surveying & Mapping (China) was installed on the top of the UAV to provide the positional information for the GPR measurements.

For the UAV-GPR system in this study, the point and route measurement modes are used. In the point measurement mode, the UAV raises the GPR antenna vertically at a slow pace, enabling GPR measurements at different antenna heights (in our case from 0 to 30 m). This mode is suitable for the calibration of GPR shape factor following the approach of Cheng et al. (2023) or for a high-accuracy survey of soil  $\xi$  at specific locations. For the route measurement mode, the antenna is carried by the UAV along the planned flight route at pre-defined heights. This method, therefore, permits mapping at the field scale. We tested the UAV-GPR method at two field sites within the riparian zone of the Yangtze River in Nanjing and farmland adjacent to the Yellow Sea in Dongtai County, Jiangsu province (Figure 4a).

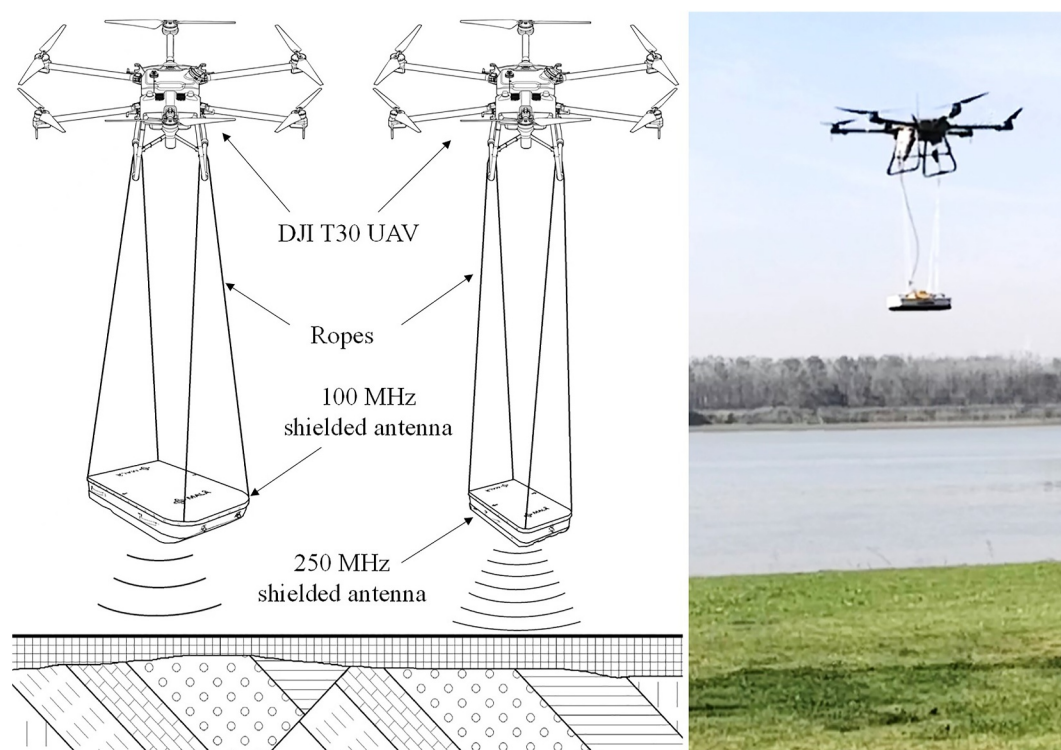


**Figure 3.** UAV-GPR system: (a) sketch of configuration separately carrying 100 and 250 MHz shielded antennas; (b) prototype system in operation with 250 MHz shielded antenna in the riparian zone of the Yangtze River.

### 3.1. Field Site 1: Riparian Zone

The first field test area is located in the riparian zone of the Yangtze River in Nanjing, China (Figure 4a). The soil type in the test area is loamy sand. On 18 November 2023, we used the UAV to take aerial photos in this area, then we employed the DJI Terra software to generate an orthophoto (Figure 4b) and a digital surface model (DSM, Figure 4c). Figure 4b indicates that the study area comprises three distinct zones: fresh water body (i.e., Yangtze River), bare land (i.e., intertidal zone), and grassland. The DSM in Figure 4c shows that the topography in the study area is relatively steep, as the elevation gradually increases along the survey line with the altitude difference of 5 m. The  $\sigma$  and temperature in the Yangtze River (adjacent to the survey area, and at the time of surveying) were about 30.4 m S/m and 21.6°C, respectively.

Firstly, in order to estimate the  $k$  of the GPR, we tested the UAV-GPR system (separately using 250 and 100 MHz antennas) over the water surface (of the Yangtze River) by carrying out measurements at a range of elevations, that is, the point method detailed earlier, since the specific electromagnetic features of fresh water are known (i.e.,  $\xi = 0.8$ ). Next, we programmed six parallel flight routes with a spacing of 10 m, perpendicular to the shoreline of the river. As the 100 MHz antenna is heavy, its flight velocity was set to 7.0 m/s, whereas the flight velocity of 250 MHz antenna was set to 2.0 m/s. The flight speed setting is related to endurance: the heavier the antenna, the shorter the UAV's flight time, so a higher flight speed is required. The time interval of GPR records was consistently set to 0.1 s. In order to reduce the effect of GPR random measurement errors, we repeated the survey with 5 flight heights above the Yangtze River surface, that is, 25, 20, 17, 15, and 13 m for 100 MHz antenna, and 20, 16, 12, 10, and 8 m for 250 MHz antenna.

In order to compare the UAV-GPR derived values with independent measurements, we used a conventional in situ sensor: a Stevens® HydraProbe dielectric impedance meter with a 5.7 cm probe length and 50 MHz operation frequency. These measurements were vertically inserted the probe into the surface soil and taken along three selected flight routes (Figure 4b, symbols) with a spacing of 20 m. At approximately 5 m intervals along these lines, we measured the soil  $\epsilon_r$  (and thus soil water content) and  $\sigma$  simultaneously using the Hydraprobe. The HydraProbe survey lines are numbered sequentially from top to bottom as 1, 2 and 3 in Figure 4b. Given the

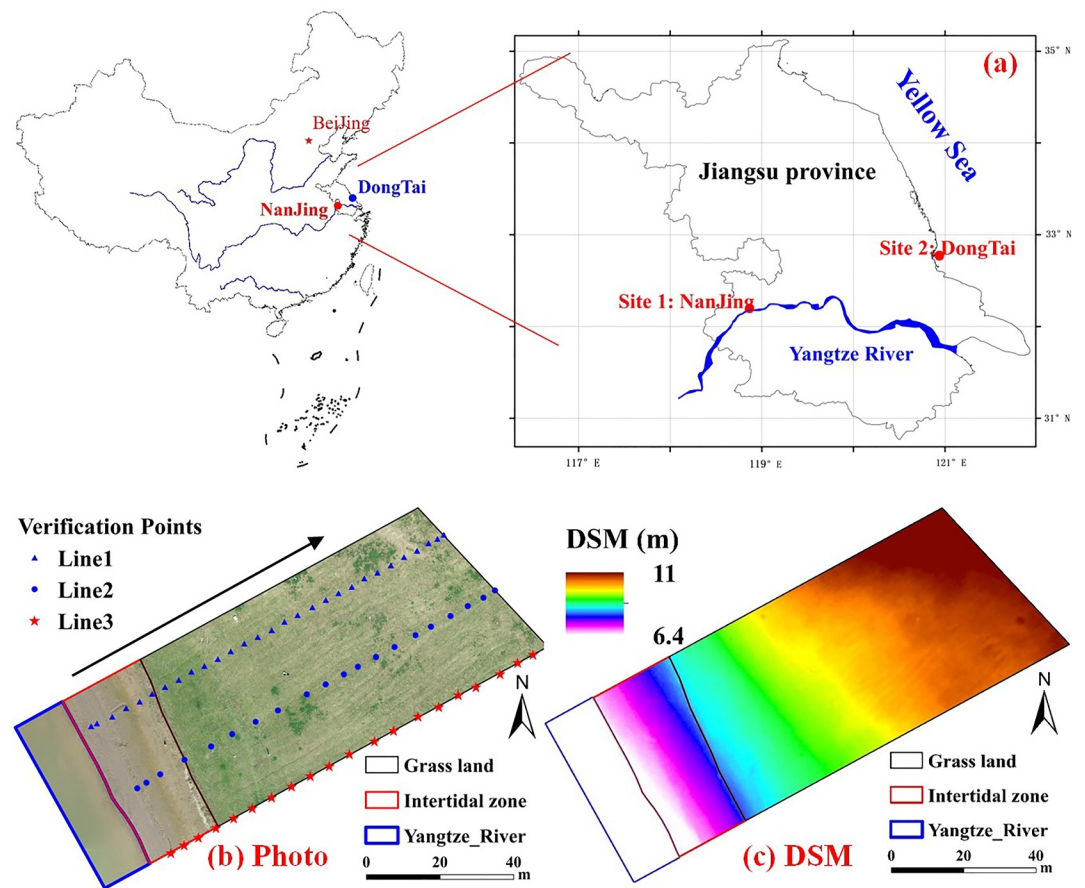


**Figure 4.** Location and geographic features of the riparian zone: (a) location; (b) aerial orthophoto; (c) digital surface model (DSM). The water body is demarked by a blue line. The HydraProbe survey lines are numbered as 1, 2 and 3 sequentially from top to bottom. The black arrowed line shows the UAV-GPR survey direction.

shallow depth of investigation of the Hydraprobe (5.7 cm), we recognize that further challenges exist in comparing measurements with those derived from the GPR surveys. The root mean square error (RMSE) and the relative error ( $R_e$ ) were used to compare the GPR results with the HydraProbe measurements:

$$\text{RMSE} = \sqrt{\frac{1}{n} \sum_{i=1}^n (y_{\text{GPR},i} - y_{\text{H},i})^2}, \quad (15)$$

$$R_e = \frac{\text{RMSE}}{\bar{y}_{\text{H}}}, \quad (16)$$

where  $n$  is the number of measurements;  $y_{\text{GPR},i}$  and  $y_{\text{H},i}$  are the  $i$ th measurement of GPR and HydraProbe taken directly beneath the UAV-GPR, respectively; and  $\bar{y}_{\text{H}}$  is the average value of HydraProbe measurements.

### 3.2. Field Site 2: Salinized Farmland

In order to test the UAV-GPR method further, a second site was selected. The site is a farmland close to the Yellow Sea at Dongtai, China (Figure 4a). The test area was formerly part of the beach of the Yellow Sea, thus providing a site with relatively high soil EC. The main soil type at the site is loam. On 06 January 2024, we used the UAV to capture aerial photos in this area, subsequently employing DJI Terra software to generate an orthophoto (Figure 5a) and a DSM (Figure 5b). Figure 5a illustrates that the study area contained wheat crops at the time of the survey. The wheat on the south side appeared notably stunted compared to that on the north side, as shown in the larger version of Figure 5a. The normalized difference vegetation index (NDVI, collected by

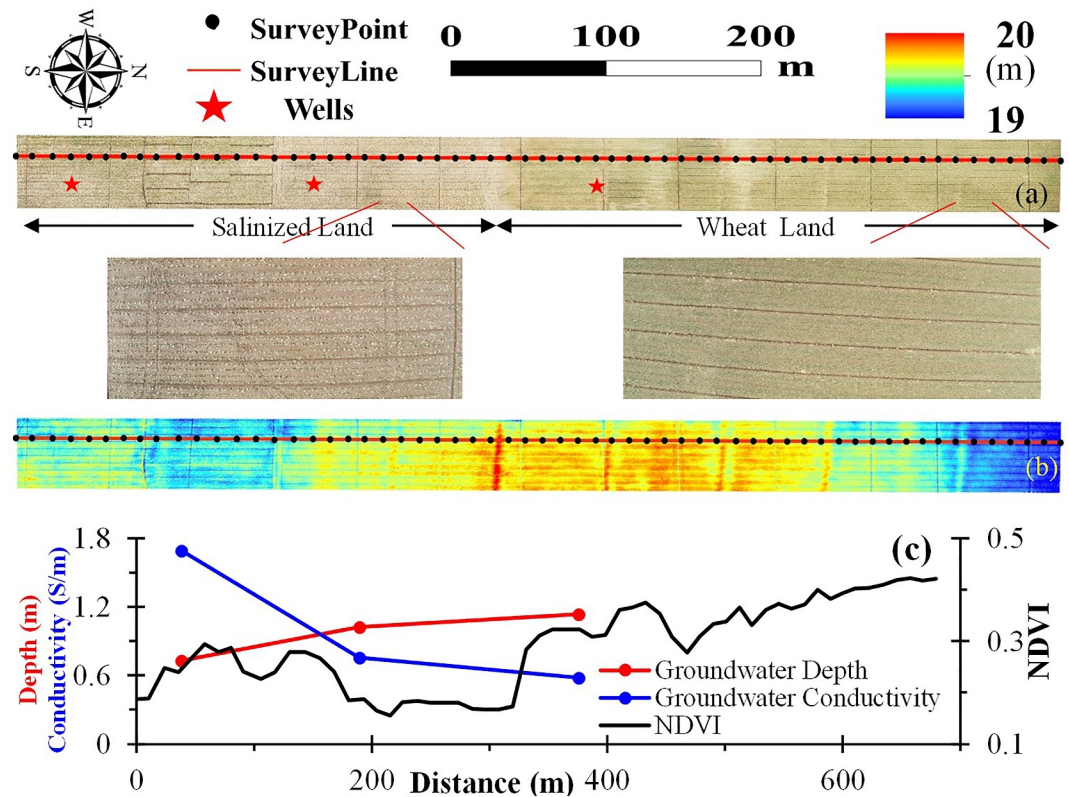


**Figure 5.** Geographic features of the salinized farmland: (a) aerial orthophoto; (b) digital surface model; (c) the observed groundwater depth and conductivity in the wells and NDVI values along the survey line. The red survey line is the flight route of UAV-GPR. The black symbols are the survey points of HydraProbe and specialized conductivity sensor.

Sentinel-2 Satellite at the time of the survey) values along the survey line (Figure 5c) also highlight the distinct differences in vegetation coverage between the south and north parts, likely because of the salinization of soil. We can, therefore, divide the farmland into two parts: salinized land and wheat land. The DSM in Figure 5b shows that the topography in the study area is relatively flat.

At the site there are three observation wells (Figure 5a); observed data (Figure 5c) show that the groundwater depth generally increases along the survey line (from south to north), ranging from 0.7 to 1.2 m. By contrast, the groundwater  $\sigma$  clearly decreases from 1.7 to 0.6 S/m. In the southern area of the site, the shallow groundwater level and high salinity groundwater are likely to be a result of soil salinization. The  $\sigma$  and temperature in the Yellow Sea (adjacent to the site and at the time of surveying) were about 2.65 S/m and 6.6°C, respectively.

In this test area, we programmed a long flight route (Figure 5), parallel to the ridge of the farmland. The flight velocities of the UAV-GPR with 100 and 250 MHz antennas were set to 7.0 and 6.0 m/s, respectively. Heavier antennas reduce the UAV's flight time, requiring adjustments in flight speed to ensure complete area coverage within the limited battery life. The time interval of GPR records was uniformly set to 0.1 s. The flight height employed for the 100 MHz antenna was 18 m, while for the 250 MHz antenna, two flight heights (8 and 12 m) were used for repeated measures. Along the flight route (Figure 5a, black symbols) with a spacing of 11.5 m, we measured the soil  $\epsilon_r$  (and thus soil water content) and  $\sigma$  simultaneously using the HydraProbe meter. As there may be high measurement errors of HydraProbe in the salinized land (Diekmann, 2023; Wilson et al., 2024), a specialized  $\sigma$  sensor TR-6D from SOONDA® (more suitable for high  $\sigma$ ) was also used at the survey points to measure the soil  $\sigma$ .

In order to measure the  $\epsilon_r$  and  $\sigma$  of sea water, we also employed the UAV-GPR system (separately using 250 and 100 MHz antennas) over the water surface of the adjacent Yellow Sea to carry out measurements at a range of elevations, that is, utilizing the point method detailed earlier.

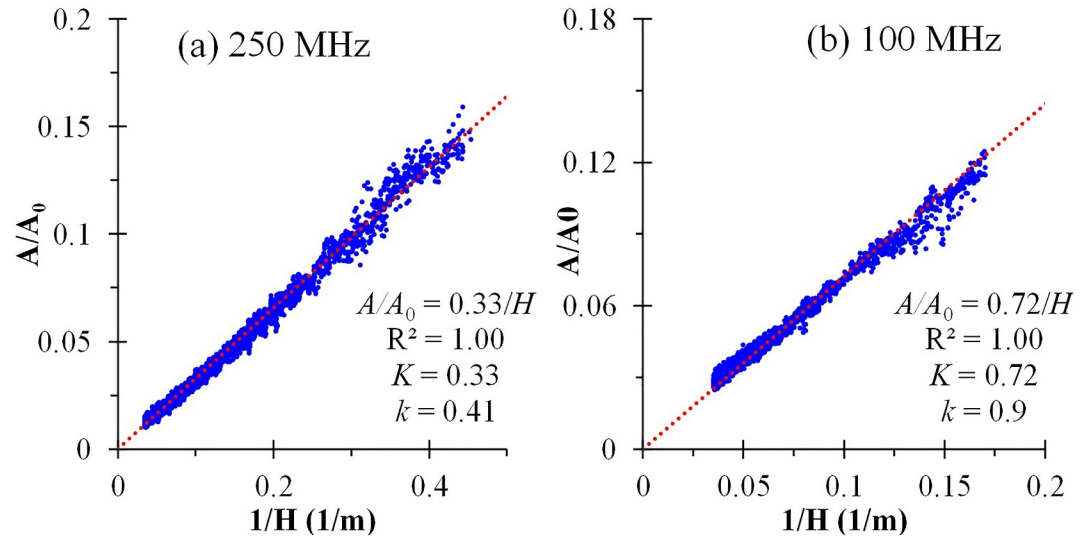


**Figure 6.** The ratio of the reflected to the air wave amplitudes ( $A/A_0$ ) versus the reciprocal of GPR height ( $1/H$ ) over the fresh water surface: (a) Mala 250 MHz shielded antenna; (b) Mala 100 MHz shielded antenna. The red dashed lines represent the linear trend lines with an intercept of 0.

## 4. Results

### 4.1. Field Experiments of Multi-Elevation GPR in Field Site 1

#### 1. Estimation of GPR shape factor by point measurement mode

As described earlier, in order to implement the multi-elevation measurements in the point measurement method, the 250 and 100 MHz shield antennas were separately raised by the DJI T30 vertically (at a velocity of 0.1 m/s) over the fresh water body (Yangtze River), while the GPR system continuously recorded data at an interval of 0.1 s. The field investigation results of the UAV-GPR system operating in point measurement mode at the Yangtze River surface are shown in Figure 6. This figure demonstrates a clearly linear relationship between the reflected and air wave amplitude ratios ( $A/A_0$ ) and the reciprocal values of GPR heights ( $1/H$ ), in accordance with the theory developed by Cheng et al. (2023).

According to Equation 10, the shape factor can be determined using the following expression:

$$k = \frac{A_0 H}{\xi}, \quad (17)$$

Given that the surface  $\xi$  of freshwater is approximately 0.8, we can estimate the  $k$  for the 250 and 100 MHz antennas using Equation 17. This results in estimated shape factor values of 0.41 m for the 250 MHz antenna and 0.9 m for the 100 MHz antenna.

#### 2. Route measurement mode for spatial scanning investigations

Based on the GPR measurements at five flight heights, the surface soil  $\xi$  values for 250 and 100 MHz antennas at a given location can be calculated using Equation 10 and subsequently interpolated to derive their spatial distributions, as shown in Figures 7a and 7b. These figures show that the  $\xi$  values of the water body measured by both antennas are close to the theoretical value of 0.8. And the  $\xi$  values generally decrease with increasing distance from the Yangtze River.

Figure 7c presents a comparison of measurements for 250 and 100 MHz antennas. This figure demonstrates a strong consistency between the measurements from both antennas, with most  $\xi$  values estimated using the 250 MHz antenna being lower than those from the 100 MHz antenna. Utilizing the  $\epsilon_r$  and  $\sigma$  values measured by the HydraProbe, we applied the Fourier transform model (Figure 1) to estimate surface reflection values. We then compared these estimated results with GPR measurements taken at the verification points (Figure 7d). This figure

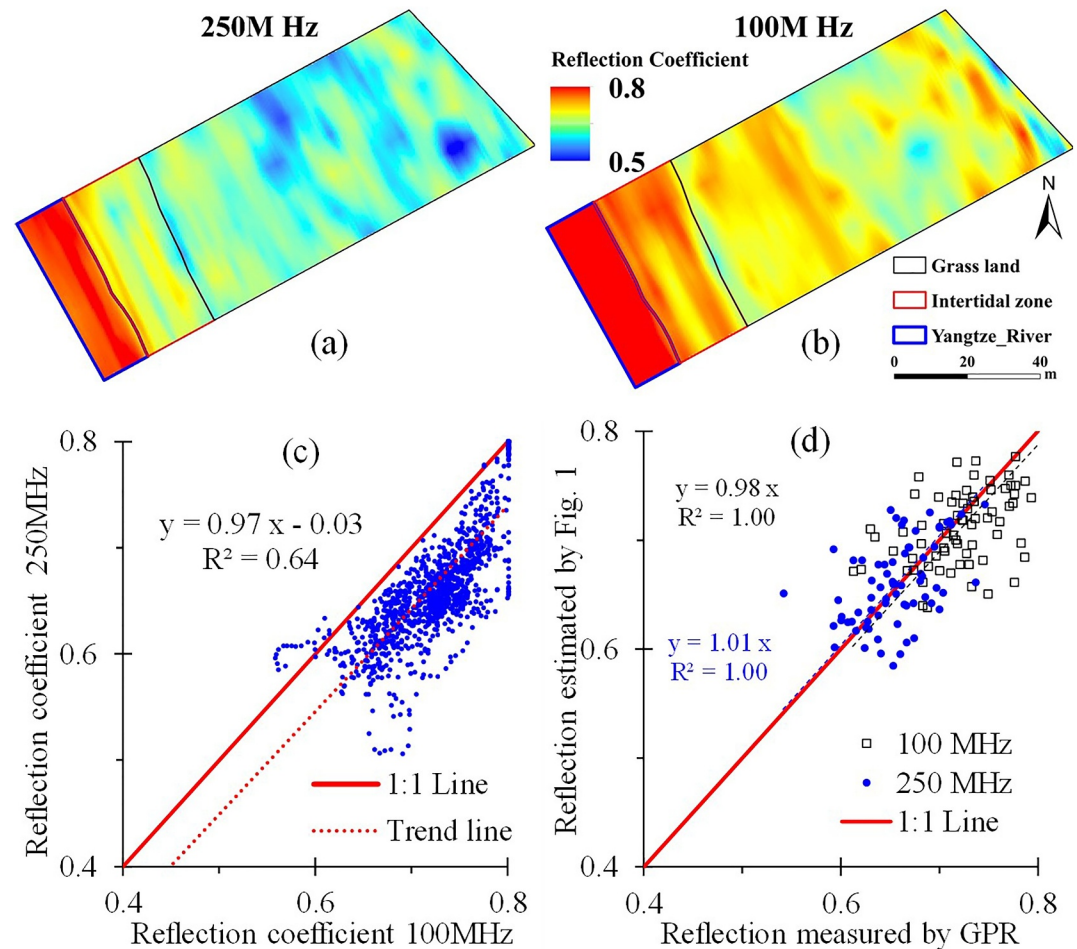


**Figure 7.** Surface soil reflection coefficient measured by UAV-GPR: (a) reflection coefficient spatial distribution measured by 250 MHz antenna; (b) reflection coefficient spatial distribution measured by 100 MHz antenna; (c) comparison of surface reflection coefficient measured by 250 and 100 MHz antennas; (d) comparison of surface reflection coefficient estimated by Fourier transform model (as shown in Figure 1, based on the relative permittivity and the electrical conductivity values are measured by HydraProbe) and measured by UAV-GPR.

indicates that most symbols cluster around the 1:1 line, and the RMSE between the measured and forward modeled (Figure 1)  $\xi$  is 0.043 and 0.039 for the 100 and 250 MHz antennas, respectively, suggesting that the UAV-GPR measurements closely align with the estimations derived from in situ investigations using the HydraProbe. In summary, the UAV-GPR measurement results appear to be both reasonable and reliable.

Based on the  $\xi$  values measured by 250 and 100 MHz antennas, both  $\epsilon_r$  and  $\sigma$  can be estimated by the least squares method according to the flow chart in Figure 2. The final results of these estimations are displayed in Figures 8a and 8b. These figures show that the  $\epsilon_r$  values in the water body zone are high and close to the theoretical values (i.e., 80). Moreover, the  $\epsilon_r$  values in the intertidal zone are generally greater than those in the grassland. A possible reason is that the low altitude areas are more susceptible to the influence of the Yangtze River. In contrast, the  $\sigma$  values in the water body are clearly lower than those in the grassland, which are generally lower than those in the intertidal zone.

We compared  $\epsilon_r$  and  $\sigma$  estimated by UAV-GPR with those measured by the HydraProbe meter at the verification points shown in Figures 8c and 8d. These figures reveal that most points fall around the 1:1 line, meaning that the GPR measurements are close to the in situ investigations. The misfit indicator (RMSE) of  $\epsilon_r$  and  $\sigma$  are 7.7 and 0.031 S/m, respectively, and the relative errors are 0.33 and 0.46, respectively.

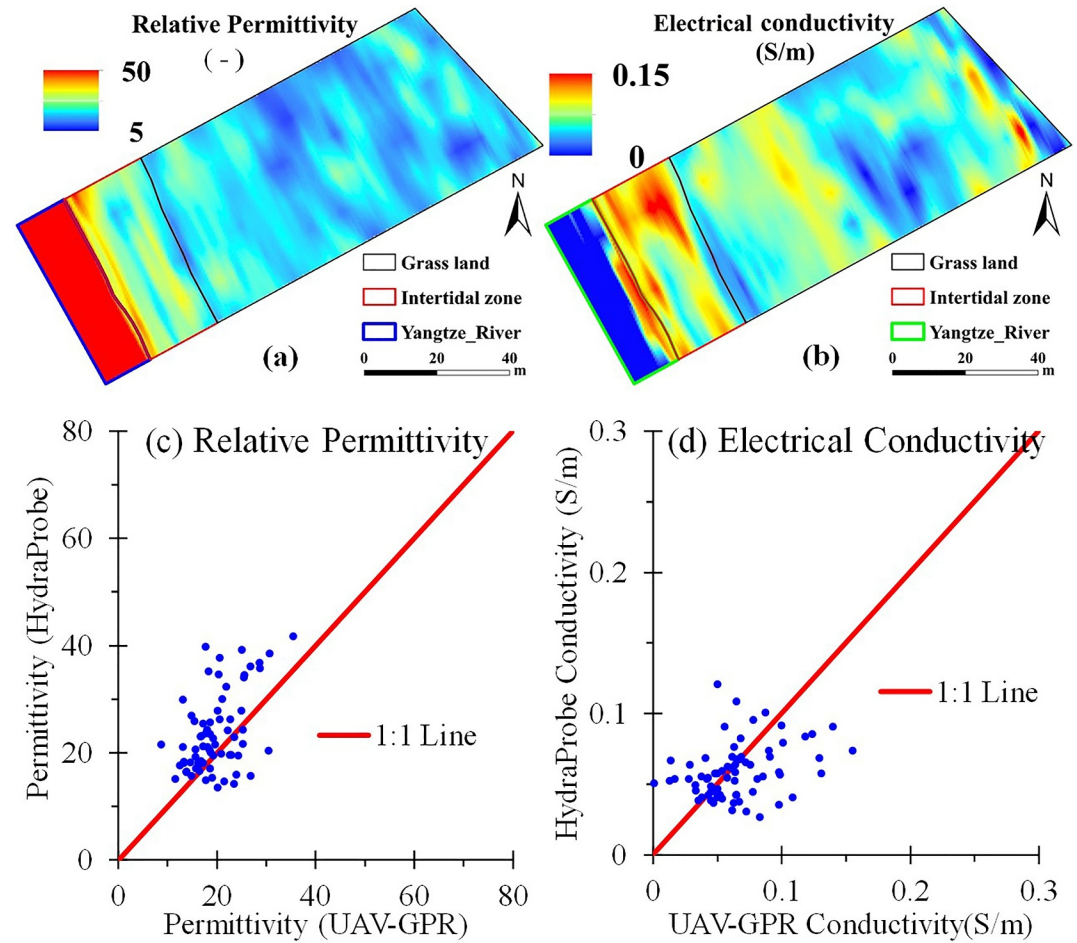


**Figure 8.** UAV-GPR survey results: (a) the spatial distribution of measured relative permittivity; (b) the spatial distribution of measured electric conductivity; (c) comparison of relative permittivity measured by UAV-GPR and by the Hydraprobe meter; (d) comparison of electric conductivity measured by UAV-GPR and by the Hydraprobe meter.

A comparison of  $\epsilon_r$  and  $\sigma$  measured by UAV-GPR and Hydraprobe along the survey lines is shown in Figure 9. This figure shows that the estimation results of UAV-GPR generally match those of the Hydraprobe. The measured  $\epsilon_r$  values tend to decrease with the distance away from the Yangtze River, possibly because the increase of the elevation results in the decrease of soil water content. By contrast, as more factors (e.g., soil water content, texture, etc.) can affect the value of  $\sigma$ , the  $\sigma$  values appear more random along the survey line.

According to the measured  $\epsilon_r$  and  $\sigma$  by UAV-GPR, the soil water content and the  $\sigma$  of pore water can be estimated separately using Equations 12 and 13, as shown in Figure 10. This shows that the apparent soil water content values in the water body are close to the theoretical value (i.e., 1.0). By contrast, because of the fresh water in the Yangtze River, the fluid  $\sigma$  values in the Yangtze River are lowest.

#### 4.2. Field Experiments of UAV-GPR at Field Site 2

##### 1. Estimation of permittivity and electric conductivity of sea water by point measurement mode

The UAV-GPR with point measurement mode (as described earlier) was used to investigate the surface reflection coefficient of sea water over the Yellow Sea. The field investigation results of the reflected and air wave amplitude ratios ( $A/A_0$ ) versus the reciprocal values of GPR heights ( $1/H$ ) are presented in Figure 11. This figure shows a clearly linear relationship between  $A/A_0$  and  $1/H$ , which, again, is in agreement with Cheng et al. (2023). According to the ratio between  $A/A_0$  and  $1/H$  in Figure 11 and the estimated shape factor over fresh water in Figure 6, we can use Equation 10 to calculate the surface reflection coefficient of sea water for 250 and 100 MHz

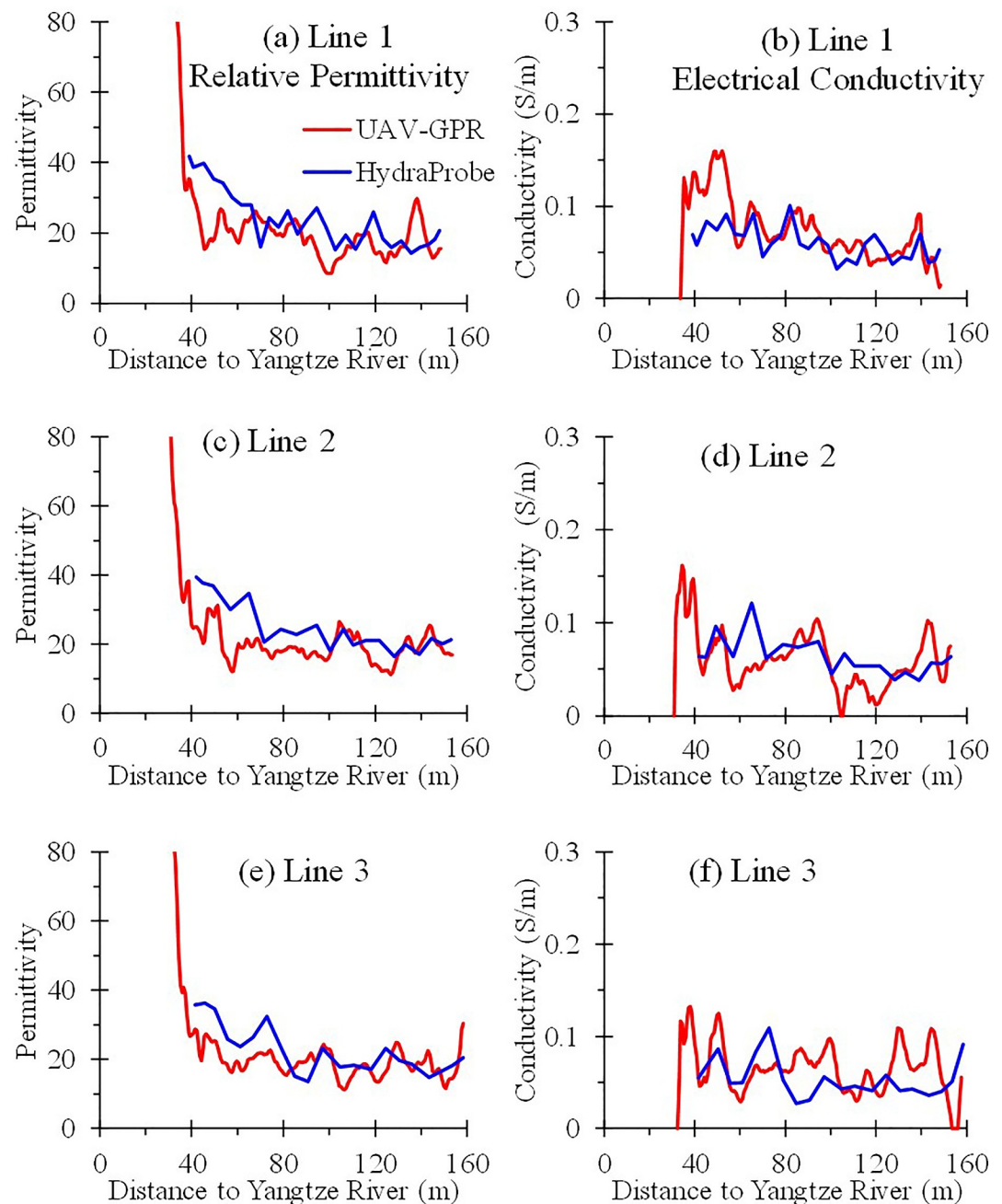


**Figure 9.** Comparison of the relative permittivity and electric conductivity measured by UAV-GPR and by Hydraprobe along the three survey lines (Figure 4). The distance refers to the length away from the Yangtze River.

antennas, separately. The estimated surface  $\xi$  values are 0.9 and 0.95, respectively, which are obviously greater than that of fresh water (i.e., 0.8) due to the effect of high salinity.

Based on the measured surface  $\xi$  of sea water, the  $\epsilon_r$  and  $\sigma$  of sea water can be estimated by the least squares method as outlined in the flow chart in Figure 2. The optimized values of  $\epsilon_r$  and  $\sigma$  are 84 and 2.7 S/m, respectively. The estimated  $\sigma$  closely matches the conductivity meter measurement (2.65 S/m).

## 2. Route measurement mode for farmland investigations

Based on the GPR measurements, the surface soil  $\xi$  values for 250 and 100 MHz antennas at investigation points were separately calculated by Equation 10, as shown in Figure 12. This figure shows that the surface soil  $\xi$  values

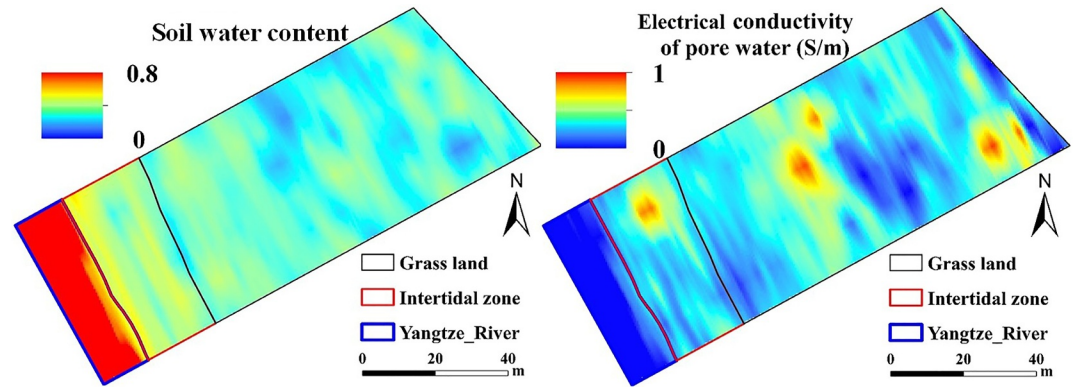


**Figure 10.** Spatial distributions of soil water content and electrical conductivity of pore water estimated by UAV-GPR: (a) Soil water content; (b) Electrical conductivity of pore water.

measured by 100 MHz antenna are clearly greater than those by 250 MHz antenna, and in the salinized land, the surface  $\xi$  values are generally greater than these in the wheat covered plot. For the 100 MHz antenna, due to the effect of soil salinity, the soil  $\xi$  values in the salinized land typically exceed 0.8 (i.e., the  $\xi$  value of fresh water).

Based on the  $\xi$  values measured by 250 and 100 MHz antennas in Figure 12, the  $\epsilon_r$  and  $\sigma$  values were estimated by the least squares method according to the flow chart in Figure 2, as shown in Figures 13a and 13b, respectively. For comparison of measurement results, the measured  $\epsilon_r$  and  $\sigma$  values by the HydraProbe meter and the specialized conductivity sensor TR-6D (for high salinity) along the survey line (Figure 5) are also plotted in Figure 13. Figure 13a shows that in the salinized land, the measured  $\epsilon_r$  values are subject to fluctuation along the survey line, and exhibit several anomalously high values. In contrast, in the wheat covered plot, these values vary steadily, and the values measured by the UAV-GPR method are close to those by the HydraProbe meter. Figure 13b shows that the measured  $\sigma$  values by HydraProbe are clearly lower than those measured by UAV-GPR and TR-6D, possibly because of high measurement errors of the HydraProbe meter in saline conditions (Diekmann, 2023). In contrast, the measurement values of UAV-GPR are comparable to those of specialized conductivity sensor TR-6D. In the wheat covered plot, the  $\sigma$  values estimated by UAV-GPR generally match with those measured by other meters (i.e., HydraProbe and TR-6D).

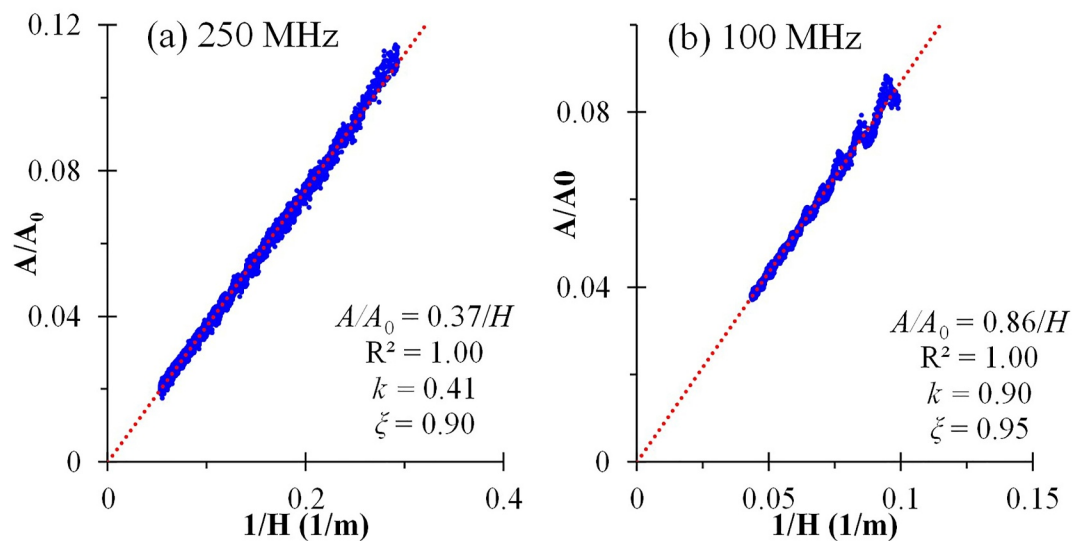


**Figure 11.** The ratio of the reflected to direct wave amplitudes ( $A/A_0$ ) versus the reciprocal of GPR height ( $1/H$ ) over the sea water surface: (a) Mala 250 MHz shielded antenna; (b) Mala 100 MHz shielded antenna. The red dashed lines represent the linear trend lines with an intercept of 0.

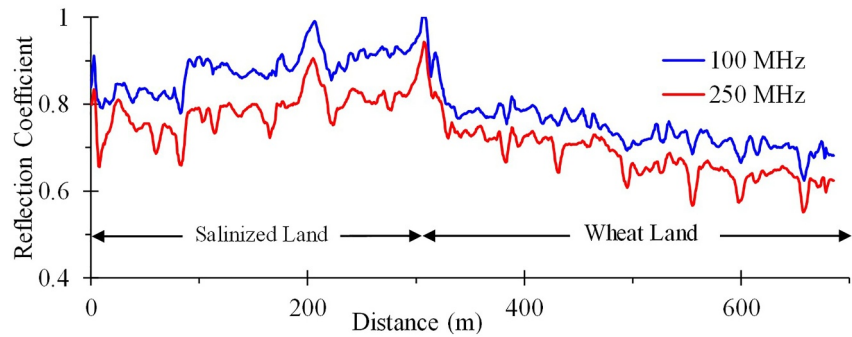


**Figure 12.** Surface soil reflection coefficient measured by UAV-GPR with 250 and 100 MHz antennas over the coastal farmland.

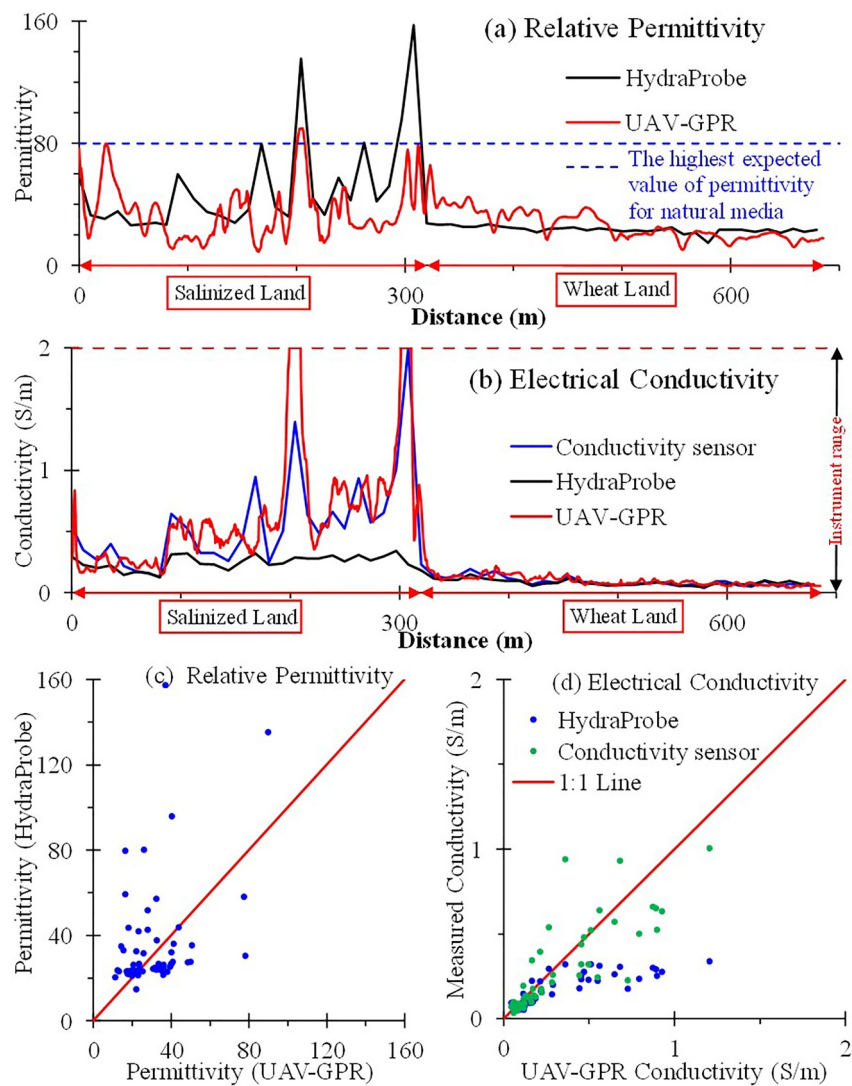


**Figure 13.** Comparison of the relative permittivity and electrical conductivity measured by UAV-GPR and by Hydraprobe meter and TR-6D conductivity sensor along the survey line (Figure 5): (a) relative permittivity; (b) electrical conductivity; (c) relative permittivity measured by UAV-GPR versus by Hydraprobe; (d) electrical conductivity measured by UAV-GPR versus by Hydraprobe and TR-6D.

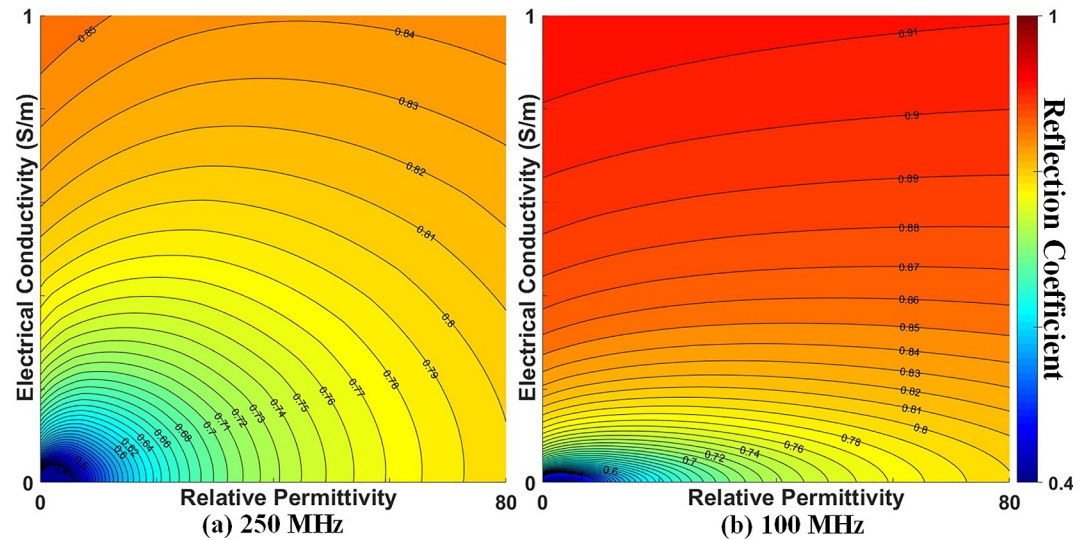


**Figure 14.** The distributions of surface reflection coefficients estimated by the Fourier transform model (Figure 1) in the parameter space at a range from 0 to 80 for relative permittivity and from 0 to 1 S/m for electrical conductivity: (a) for the 250 MHz antenna; (b) for the 100 MHz antenna.

We compared the  $\epsilon_r$  and  $\sigma$  estimated by UAV-GPR with those measured by the HydraProbe and TR-6D meters at the verification points. Figure 13c shows that most points fall around the 1:1 line, except for some anomalously large values (e.g., the  $\epsilon_r > 80$ ), again likely to be a result of HydraProbe measurements measurement inaccuracy at high salinity (Diekmann, 2023). In contrast, Figure 13d shows that the  $\sigma$  data measured by the UAV-GPR closely match those measured by the TR-6D meter. In the high  $\sigma$  area, the HydraProbe measurements obviously underestimate the  $\sigma$  values. In the low  $\sigma$  area (i.e., wheat cropped area), comparing the UAV-GPR measurements with those of the HydraProbe meter, results in an RMSE (Equation 15) for  $\epsilon_r$  and  $\sigma$  of 8.0 and 0.034 S/m, respectively, and a relative error of 0.34 and 0.41, respectively, which are similar to the values estimated in the Field Site 1.

## 5. Discussion

### 5.1. Accuracy of the UAV-GPR Method

The distributions of surface  $\xi$  values estimated by the Fourier transform model (Figure 1) in the parameter space (i.e., ranging from 0 to 80 for  $\epsilon_r$  and from 0 to 1 S/m for  $\sigma$ ) for the 250 and 100 MHz antennas are shown in Figure 14. This figure shows that for both 250 and 100 MHz antennas, the densities of  $\xi$  contour lines clearly decrease as the parameters (i.e.,  $\epsilon_r$  and  $\sigma$ ) increase, which means that the  $\xi$  values are more sensitive to  $\epsilon_r$  and  $\sigma$  at lower values of  $\epsilon_r$  and  $\sigma$ . For the 100 MHz antenna, in the high  $\sigma$  zone, the  $\xi$  values change little with  $\epsilon_r$ . In contrast, for the 250 MHz antenna, the  $\xi$  values are more sensitive to both  $\epsilon_r$  and  $\sigma$ .

In order to evaluate the measurement accuracy of the UAV-GPR method, a Monte Carlo simulation was utilized. We first calculated the  $\xi$  value using the Fourier transform model (Figure 1) at discrete points in the ( $\epsilon_r$  and  $\sigma$ ) parameter space with a range from 0 to 80 for  $\epsilon_r$  and from 0 to 1 S/m for  $\sigma$  (Figure 14). Next, assuming a measurement error of surface  $\xi$  equal to 2% (i.e., the nominal observational error specified for most typical soil-moisture instruments), for each pair of  $\epsilon_r$  and  $\sigma$  values we uniformly randomly sampled 100 realizations of reflection coefficients for the 250 and 100 MHz antennas from the ratio range of [0.98 1.02] relative to the  $\xi$  values in Figure 14. This number (i.e., 100) was chosen based on a convergence analysis, where increasing the number beyond 100 did not significantly alter the statistical distribution of the retrieved parameters. This threshold provides a balance between computational efficiency and result stability, ensuring robust uncertainty estimation without excessive computational cost. These 100 realizations were treated as the observed  $\xi$  values using UAV-GPR, and based on each set of  $\xi$  values, we estimated  $\epsilon_r$  and  $\sigma$  using the least squares algorithm (Figure 2). Finally, we computed the RMSE (i.e., similar to Equation 15) of the estimated  $\epsilon_r$  and  $\sigma$ , and evaluated the relative errors ( $Re$ ) using:

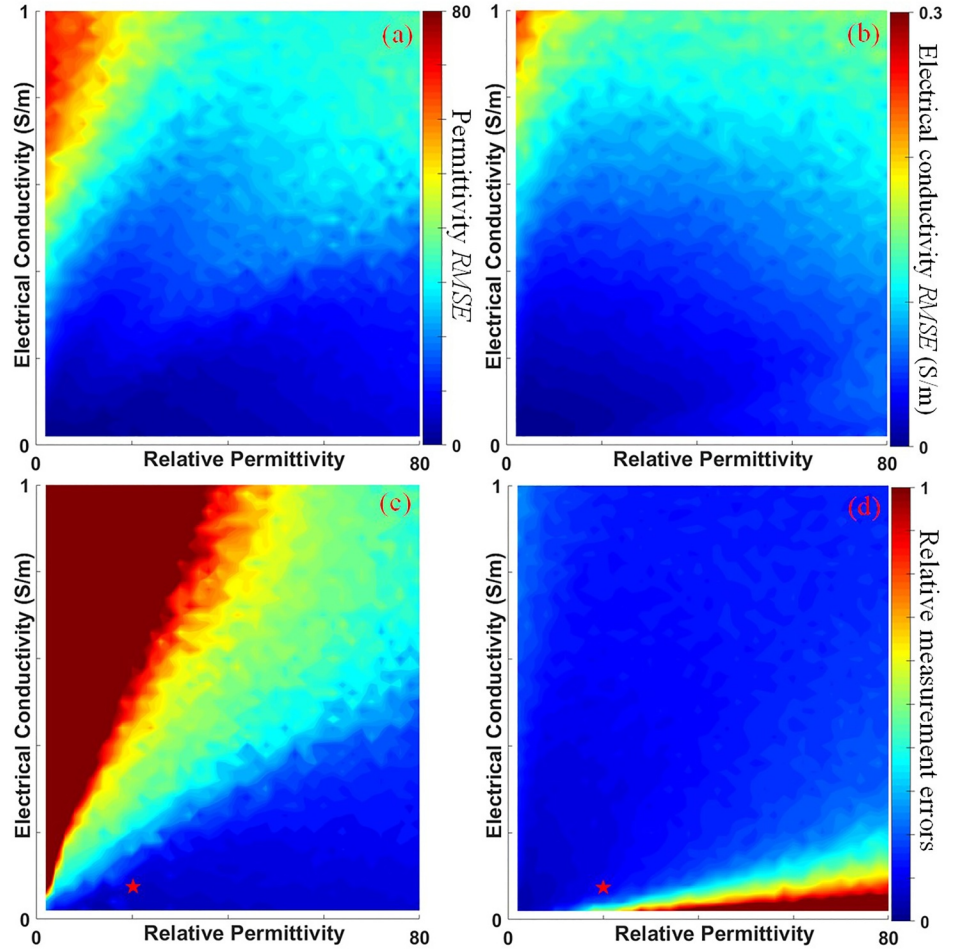


**Figure 15.** Distributions in the parameter space of root mean square error (RMSE) and relative error ( $R_e$ ) for the relative permittivity and electrical conductivity based on the synthesized data using the Monte Carlo simulation: (a) RMSE of relative permittivity; (b) RMSE of electrical conductivity; (c)  $R_e$  of relative permittivity; (d)  $R_e$  of electrical conductivity. The red star shows the location (in the parameter space) for the average values of relative permittivity and electrical conductivity measured by the in situ sensors in the riparian zone (site 1) and wheat cropped area (site 2).

$$\text{RMSE} = \sqrt{\frac{1}{n} \sum_{i=1}^n (F_i - F)^2}, \quad (18)$$

$$R_e = \frac{\text{RMSE}}{F}, \quad (19)$$

where  $F$  is the desired value of the  $\epsilon_r$  or  $\sigma$ ;  $F_i$  is the estimated value of the  $\epsilon_r$  or  $\sigma$ ;  $n$  is the number (e.g., 100) of random  $\xi$  realizations.

The distribution of computed RMSE and  $R_e$  values is shown in Figure 15, which shows that RMSE of both  $\epsilon_r$  and  $\sigma$  increases with  $\sigma$ . That is, in the low  $\sigma$  area, the measurement accuracy of UAV-GPR is higher. For the  $\epsilon_r$  (Figure 15c), in the low  $\epsilon_r$  and high  $\sigma$  area, the  $R_e$  values are clearly greater than 1, which means that the measurement accuracy of UAV-GPR for the  $\epsilon_r$  is low in the salinized land. By contrast, the measurement accuracy for  $\sigma$  is clearly higher than that for the  $\epsilon_r$  in the high  $\sigma$  area. In summary, the UAV-GPR method can relatively accurately measure the  $\epsilon_r$  in the low  $\sigma$  area (e.g., the wheat cropped area of site 2 and the riparian zone of site 1), and  $\sigma$ , except in regions characterized by low  $\sigma$  and high  $\epsilon_r$ . In the salinized land, the measurement accuracy of  $\sigma$  is clearly better than that of  $\epsilon_r$ .

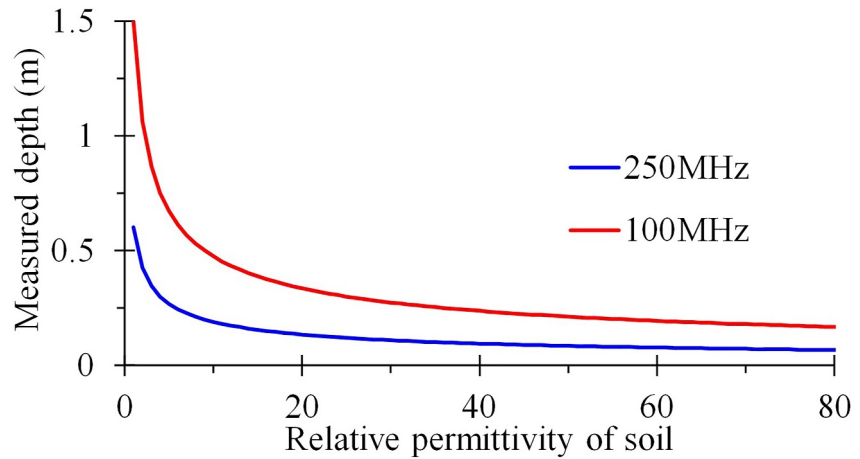


**Figure 16.** The GPR investigation depth versus the soil relative permittivity for 250 and 100 MHz antennas.

The distributions in Figure 15 are in agreement with our findings from the two field tests. In the riparian zone (first site) and the wheat cropped area (second site), because of the low  $\epsilon_r$  and  $\sigma$ , the UAV-GPR derived values match well with those measured by HydraProbe meter (Figures 8 and 13). In contrast, in the salinized land with high  $\sigma$ , the  $\epsilon_r$  values measured by UAV-GPR exhibit spurious readings (Figure 13a). However, the  $\sigma$  values measured by UAV-GPR generally match with these estimated by the specialized conductivity sensor TR-6D (Figure 13d).

## 5.2. Influence Factors of the Proposed UAV-GPR Method

There is an assumption of an ideal soil layer (i.e., smooth soil surface and homogeneous soil layer) for the multi-elevation GPR method (Cheng et al., 2023). However, in the field, the test environment is complex, and many factors (e.g., heterogeneous soil layer, soil surface roughness, crops and topography) may affect the measurement results of the UAV-GPR method. In the following text, we discuss the effect of these factors.

### 1. Investigation depth of the UAV-GPR method

In a heterogenous soil layer, the reflected GPR signals ( $A_{ref}$ ) are not only affected by the soil surface, but also by soil variability, for example, layering. According to the Fresnel principle, the reflecting zone that contributes to a single reflection can be treated as the zone of influence. In other words, the travel time of GPR signal in the zone of influence volume should be less than the period of electromagnetic wave:

$$\frac{2d}{c/\sqrt{\epsilon_r}} < \frac{1}{f}, \quad (20)$$

where  $d$  is the depth of the zone of influence, that is, the investigation depth;  $c$  is the electromagnetic velocity in the free space ( $=3 \times 10^8$  m/s).

Therefore, the investigation depth of the UAV- GPR method is:

$$d = \frac{1}{2} \frac{c}{f\sqrt{\epsilon_r}}. \quad (21)$$

Using Equation 21, the measurement depths of 250 and 100 MHz antennas as a function of soil  $\epsilon_r$  were computed and are shown in Figure 16. This figure reveals that the GPR measurement depth decreases as the  $\epsilon_r$  increase, and the investigation depth of 100 MHz antenna is about 2.5 times greater than that of the 250 MHz antenna. The average investigation depth of the 250 and 100 MHz antennas are about 0.1 and 0.3 m, respectively.

### 2. Effect of surface effects

Surface effects, including surface roughness and vegetation cover, can cause less energy being reflected in the specular direction because of the diffuse reflections of electromagnetic waves on a rough surface. Therefore, the

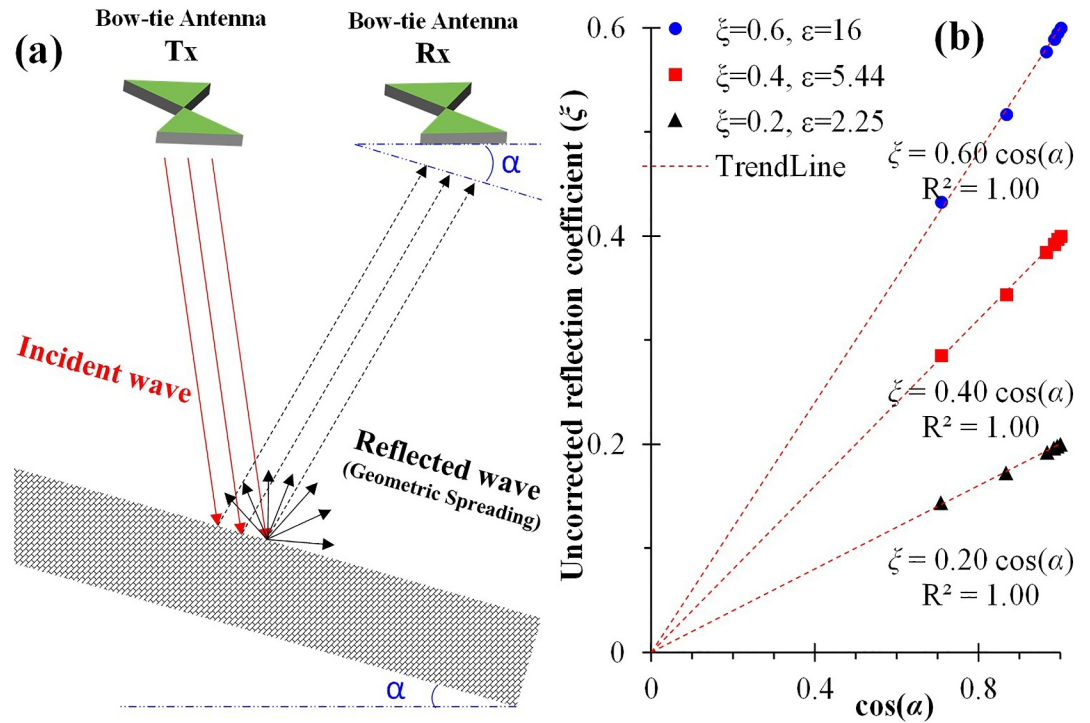


**Figure 17.** Effect of surface slope on measured surface reflection coefficient: (a) the schematic map of air-launched ground penetrating radar over the surface slope; (b) the uncorrected surface reflection coefficient versus the cosine value of surface slope. The  $\alpha$  is the angle of the slope.

surface effects could have adverse effects on UAV-GPR measurements. However, according to Rayleigh's criterion, the effect of surface roughness can be neglected when the maximum height of the surface protuberances is less than one-eighth of the GPR wavelength, which had been verified by Lambot et al. (2006). Therefore, the maximum protuberance heights allowed in the ground surface for the 250 and 100 MHz antennas in this study are about 0.15 and 0.375 m, respectively. The maximum protuberance heights estimated here based on center frequency are provided for reference only; in practice, the behavior of ultra-wideband GPR signals may be more complex.

Vegetation cover not only affects surface roughness but also, because vegetation (e.g., crops) essentially consists of water-filled tubular structures with high permittivity, influences the measured permittivity and thus surface reflection coefficient. Consequently, the impact of vegetation cover is quite complex, and there is currently no widely accepted theory to estimate its effects, warranting further research in the future.

### 3. Effect of surface slope

The antenna usually receives the electromagnetic wave best in the vertical or near vertical direction, while the oblique electromagnetic wave reaches the antenna at a large angle. When the UAV-GPR is deployed over a slope, the bow-tie antennas are not parallel to the ground surface. Consequently, the wave is incident at an oblique angle, which reduces the electric field component perpendicular to the antenna's receiving element. In other words, the effective receiving area of GPR Rx antenna is changed to the projected area of Rx antenna on the slope, rather than the actual area of the GPR Rx antenna (Figure 17a) (Chi, Pang, et al., 2024; Chi, Mao, et al., 2024). Therefore, a correction factor is necessary for UAV-GPR to measure the surface  $\xi$  on a slope (Equation 10), which is the cosine value of the slope gradient:

$$\xi_c = \frac{\xi}{\cos(\alpha)}, \quad (22)$$

where  $\alpha$  is the angle of the slope (Figure 17a);  $\xi_c$  is the corrected  $\xi$ .

In order to assess the correction factor, we built a numerical model using the gprMax software (Warren et al., 2016) with the built-in GPR antenna model (GSSI 400 MHz) to simulate the propagation of EM waves for the multi-elevation GPR method to measure the surface  $\xi$  over slopes with different gradients and soil permittivity values. The GSSI 400 MHz antenna has a low frequency similar to that of the Mala 100 and 250 MHz antennas used in the field, and all are shielded pulse GPR systems, making it well suited for testing the correction formula (Equation 22). In the numerical model, the simulated spatial domain is 2.0 m (length)  $\times$  2.0 m (width)  $\times$  2.0 m (height). The vertical dimension is split into two layers: an upper layer representing free space, and a lower layer of slope representing the studied (soil) medium (Figure 17a). The spatial and temporal discretization values are set to 0.001 m and 0.002 ns, respectively.

We chose six kinds of slope angles (i.e., 0°, 6°, 10°, 15°, 30° and 45°) and three kinds of soil materials (i.e., 2.25, 5.44, and 16  $\epsilon_r$ , corresponding to 0.2, 0.4 and 0.6 surface  $\xi$  values), which were combined into 18 different scenarios. We simulated these scenarios on the High Performance Computing Platform of Hohai University. The directly measured (i.e., uncorrected) surface  $\xi$  versus the cosine slope for different scenarios is shown in Figure 17b. This figure shows that for each soil material, there is a clearly linear relationship between the uncorrected surface  $\xi$  and the cosine slope angle, and the  $\xi$  divided by  $\cos(\alpha)$  is a constant and equal to the surface  $\xi$  of corresponding soil material. Therefore, the correction formula (Equation 22) can effectively remove the influence of surface slope for the UAV-GPR method; however, it must be acknowledged that this conclusion requires further field validation. Note that the correction formula (Equation 22) can be also used to compensate for antenna swing caused by UAV-GPR flight instability; in such cases, the flight attitude angle (which can be recorded by an inertial measurement unit (IMU)) should be used in place of the slope angle.

In this study, as the slope angles of the two field sites are less than 6°, the effect of surface slope can be ignored, and the correction formula (Equation 22) was not used.

## 6. Conclusion

We have developed a new UAV-GPR method that employs two antenna frequencies (250 and 100 MHz in our examples) to separately measure the surface  $\xi$  by a multi-elevation UAV-GPR approach. Then using the measured  $\xi$  values and a Fourier transform approach (Figure 1) combined with the least squares method, estimates of the  $\epsilon_r$  and  $\sigma$  (and thus soil water content and salinity) are made. The new method shows improvement over the original UAV-GPR method proposed by Cheng et al. (2023) by taking into account the effect of  $\sigma$  on surface  $\xi$ , and avoids the use of more complex full waveform analysis, as proposed in earlier works (Wu & Lambot, 2022).

We tested the method at two field sites: a riparian zone of the Yangtze River and a farmland close to the Yellow Sea. We compared the UAV-GPR derived values with in situ Hydraprobe meter measurements. The results show that in the low  $\sigma$  area (i.e., riparian zone of the first site and wheat cropped area of the second site), the measurement results of  $\epsilon_r$  and  $\sigma$  are all close to the Hydraprobe measurements (RMSEs are 8 and 0.03 S/m for  $\epsilon_r$  and  $\sigma$ , respectively, and the relative errors are 0.33 and 0.44, respectively). However, in the salinized area of the second site, the UAV-GPR estimates of  $\epsilon_r$  suffer from high uncertainty. Nonetheless, the  $\sigma$  values derived from UAV-GPR measurements appear more reliable than those measured by the HydraProbe meter. These findings were confirmed by an accuracy analysis using Monte Carlo simulation under the assumption of 2% measurement errors, which shows that the measurement error of  $\epsilon_r$  increases with  $\sigma$ , and the relative errors of  $\sigma$  are generally less than those of  $\epsilon_r$  except in the high  $\epsilon_r$  and low  $\sigma$  area.

In summary, the multi-elevation UAV-GPR with two different frequency antennas may provide a useful method to simultaneously measure the  $\epsilon_r$  and  $\sigma$ , offering a higher resolution than remote sensing method and better working efficiency than conventional in situ methods. The investigation depth of UAV-GPR decreases with the soil  $\epsilon_r$  increase, and the average investigation depth of 250 and 100 MHz antennas are 0.1 and 0.3 m, respectively. After employing the correction factor (i.e., the reciprocal of cosine value of slope angle), the UAV-GPR method can be used in a sloped area, and can also compensate for antenna swing caused by flight instability when the flight attitude angle is used instead of the slope angle. As the surface roughness can affect the measurement accuracy of  $\xi$ , this may limit application in sites with significant topographic features.

The use of a UAV platform for combined permittivity and electrical conductivity measurements could offer greater efficiency of geophysical surveying and may have immense value for investigating areas with restricted or

challenging access, for example, wetlands. Given the growing use of UAVs to support geophysical measurements, we expect to see further development and application of the method proposed here.

## Conflict of Interest

The authors declare no conflicts of interest relevant to this study.

## Data Availability Statement

The data used in this paper is accessible at (Cheng, 2025).

## Acknowledgments

This research was funded by the National Key Research and Development Program of China (Grant 2022YFC3202301), the Key Technologies Research on Development and Service of Yellow River Simulator for Super-Computing Platform (Grant 201400210900), YRCC Outstanding Young Talents Sci-Tech Project (Grant HQK-202304), the Second Tibetan Plateau Scientific Expedition and Research Program (STEP; Ministry of Science and Technology, MOST; Grant 2019QZKK0207-02), and the National Natural Science Foundation of China (Grants 42030506, U21A2004, 52179013, and 42071039). We are grateful to the Associate Editor and three anonymous reviewers for their constructive comments on an earlier version of the manuscript.

## References

- Acharya, B. S., Bhandari, M., Bandini, F., Pizarro, A., Perks, M., Joshi, D. R., et al. (2021). Unmanned aerial vehicles in hydrology and water management: Applications, challenges, and perspectives. *Water Resources Research*, 57(11), e2021WR029925. <https://doi.org/10.1029/2021wr029925>
- Andreasen, M., Jensen, K. H., Desilets, D., Franz, T. E., Zreda, M., Bogen, H. R., & Looms, M. C. (2017). Status and perspectives on the cosmic-ray neutron method for soil moisture estimation and other environmental science applications. *Vadose Zone Journal*, 16(8), vzj2014–vzj2017. <https://doi.org/10.2136/vzj2017.04.0086>
- Babaeian, E., Sadeghi, M., Jones, S. B., Montzka, C., Vereecken, H., & Tuller, M. (2019). Ground, proximal, and satellite remote sensing of soil moisture. *Reviews of Geophysics*, 57(2), 530–616. <https://doi.org/10.1029/2018rg000618>
- Brocca, L., Ciabatta, L., Massari, C., Camici, S., & Tarpanelli, A. (2017). Soil moisture for hydrological applications: Open questions and new opportunities. *Water*, 9(2), 140. <https://doi.org/10.3390/w9020140>
- Brovelli, A., & Cassiani, G. (2011). Combined estimation of effective electrical conductivity and permittivity for soil monitoring. *Water Resources Research*, 47(8), W08510. <https://doi.org/10.1029/2011wr010487>
- Butcher, K., Wick, A. F., DeSutter, T., Chatterjee, A., & Harmon, J. (2016). Soil salinity: A threat to Global food security. *Agronomy Journal*, 108(6), 2189–2200. <https://doi.org/10.2134/agronj2016.06.0368>
- Cheng, Q. (2025). Original data for “Combined measurement of soil permittivity and electrical conductivity using UAV-based ground penetrating radar” [Dataset]. *Figshare*. <https://doi.org/10.6084/m9.figshare.29205452.v2>
- Cheng, Q., Su, Q., Binley, A., Liu, J., Zhang, Z., & Chen, X. (2023). Estimation of surface soil moisture by a multi-elevation UAV-based ground penetrating radar. *Water Resources Research*, 59(2), e2022WR032621. <https://doi.org/10.1029/2022wr032621>
- Chi, Y., Mao, L., Wang, X., Pang, S., & Yang, Y. (2024). Three-dimensional numerical simulation and experimental validation of airborne ground-penetrating radar based on CNCS-FDTD method under undulating terrain conditions. *SCI REP-UK*, 14(1), 22156. <https://doi.org/10.1038/s41598-024-73375-y>
- Chi, Y., Pang, S., Mao, L., & Zhou, Q. (2024). Research on airborne ground-penetrating radar imaging technology in complex terrain. *Remote Sensing*, 16(22), 4174. <https://doi.org/10.3390/rs16224174>
- Corwin, D. L. (2008). Past, present, and future trends in soil electrical conductivity measurements using geophysical methods. In *Handbook of agricultural geophysics* (pp. 17–44).
- Corwin, D. L., & Yemoto, K. (2019). Measurement of soil salinity: Electrical conductivity and total dissolved solids. *Soil Science Society of America Journal*, 83(1), 1–2. <https://doi.org/10.2136/sssaj2018.06.0221>
- Dehem, M. (2020). *Soil moisture mapping using a drone-borne Ground Penetrating Radar*. Université catholique de Louvain.
- Diekmann, A. (2023). Soil moisture sensing in saltwater: A review. *Environmental Earth Sciences*, 82(20), 478. <https://doi.org/10.1007/s12665-023-11188-4>
- Hilhorst, M. A. (2000). A pore water conductivity sensor. *Soil Science Society of America Journal*, 64(6), 1922–1925. <https://doi.org/10.2136/sssaj2000.6461922x>
- Lambot, S., Antoine, M., Vanclooster, M., & Slob, E. C. (2006). Effect of soil roughness on the inversion of off-ground monostatic GPR signal for noninvasive quantification of soil properties. *Water Resources Research*, 42(3), W03403. <https://doi.org/10.1029/2005wr004416>
- Lambot, S., Bosch, I. v. d., Stockbroeckx, B., Druyts, P., Vanclooster, M., & Slob, E. (2005). Frequency dependence of the soil electromagnetic properties derived from ground-penetrating radar signal inversion. *Subsurface Sensing Technologies and Applications*, 6(1), 73–87. <https://doi.org/10.1007/s11220-005-4228-x>
- Lambot, S., Slob, E., van den Bosch, I., Stockbroeckx, B., & Vanclooster, M. (2004). Modeling of ground-penetrating Radar for accurate characterization of subsurface electric properties. *IEEE T GEOSCI REMOTE*, 42(11), 2555–2568. <https://doi.org/10.1109/tgrs.2004.834800>
- Lopez, Y. A., García-Fernández, M., Álvarez-Narciandi, G., & Andrés, F. L. H. (2022). Unmanned aerial vehicle-based ground-penetrating radar systems: A review. *IEEE GEOSCI REM SENS M*, 10(2), 66–86. <https://doi.org/10.1109/mgrs.2022.3160664>
- Mane, S., Das, N., Singh, G., Cosh, M., & Dong, Y. (2024). Advancements in dielectric soil moisture sensor calibration: A comprehensive review of methods and techniques. *COMPUT ELECTRON AGR*, 218, 108686. <https://doi.org/10.1016/j.compag.2024.108686>
- Metternicht, G. I., & Zinck, J. A. (2003). Remote sensing of soil salinity: Potentials and constraints. *Remote Sensing of Environment*, 85(1), 1–20. [https://doi.org/10.1016/S0034-4257\(02\)00188-8](https://doi.org/10.1016/S0034-4257(02)00188-8)
- Mu, W., Han, N., Qu, Z., Zheng, M., Shan, Y., Guo, X., et al. (2024). ECWS: Soil salinity measurement method based on electrical conductivity and moisture content. *Agronomy*, 14(7), 1345. <https://doi.org/10.3390/agronomy14071345>
- Petropoulos, G. P., Ireland, G., & Barrett, B. (2015). Surface soil moisture retrievals from remote sensing: Current status, products & future trends. *Physics and Chemistry of the Earth, Parts A/B/C*, 83–84, 36–56. <https://doi.org/10.1016/j.pce.2015.02.009>
- Rhoades, J. D. (1993). Electrical conductivity methods for measuring and mapping soil salinity. In D. L. Sparks (Ed.), *Advances in Agronomy* (pp. 201–251). Academic Press. [https://doi.org/10.1016/S0065-2113\(08\)60795-6](https://doi.org/10.1016/S0065-2113(08)60795-6)
- Robinson, D. A., Jones, S. B., Wraith, J. M., Or, D., & Friedman, S. P. (2003). A review of advances in dielectric and electrical conductivity measurement in soils using time domain reflectometry. *Vadose Zone Journal*, 2(4), 444–475. <https://doi.org/10.2136/vzj2003.4440>
- Scott, J. H. (1983). Electrical and magnetic properties of rock and soil Open-File Report 83-915. U.S. Geological Survey. <https://doi.org/10.3133/ofr83915>

- Seneviratne, S. I., Corti, T., Davin, E. L., Hirschi, M., Jaeger, E. B., Lehner, I., et al. (2010). Investigating soil moisture – Climate interactions in a changing climate: A review. *Earth-Science Reviews*, 99(3), 125–161. <https://doi.org/10.1016/j.earscirev.2010.02.004>
- Shamshiri, R. R., Balasundram, S. K., Rad, A. K., Sultan, M., & Hameed, I. A. (2022). An overview of soil moisture and salinity sensors for digital agriculture applications. In R. Shamshiri & S. Shafian (Eds.), *Digital Agriculture, Methods and Applications* (pp. 129–154). IntechOpen.
- Slob, E., & Fokkema, J. (2002). Coupling effects of two electric dipoles on an interface. *Radio Science*, 37(5), 1–6. <https://doi.org/10.1029/2001rs002529>
- Srivastava, P., Wu, Q.-S., & Giri, B. (2019). Salinity: An overview. In B. Giri & A. Varma (Eds.), *Microorganisms in Saline Environments: Strategies and Functions* (pp. 3–18). Springer International Publishing.
- Susha Lekshmi, S. U., Singh, D., & Shojaei Baghini, M. (2014). A critical review of soil moisture measurement. *Measurement*, 54, 92–105. <https://doi.org/10.1016/j.measurement.2014.04.007>
- Topp, G. C., Davis, J. L., & Annan, A. P. (1980). Electromagnetic determination of soil water content: Measurements in coaxial transmission lines. *Water Resources Research*, 16(3), 574–582. <https://doi.org/10.1029/wr016i003p00574>
- Tran, A. P., Ardekani, M. R. M., & Lambot, S. (2012). Coupling of dielectric mixing models with full-wave ground-penetrating radar signal inversion for sandy-soil-moisture estimation. *Geophysics*, 77(3), H33–H44. <https://doi.org/10.1190/geo2011-0100.1>
- Tran, A. P., André, F., & Lambot, S. (2014). Validation of near-field ground-penetrating radar modeling using full-wave inversion for soil moisture estimation. *IEEE T GEOSCI REMOTE*, 52(9), 5483–5497. <https://doi.org/10.1109/TGRS.2013.2289952>
- Tulaczyk, S. M., & Foley, N. T. (2020). The role of electrical conductivity in radar wave reflection from glacier beds. *The Cryosphere*, 14(12), 4495–4506. <https://doi.org/10.5194/tc-14-4495-2020>
- Turner, W. (2014). Sensing biodiversity. *SCIENCE*, 346(6207), 301–302. <https://doi.org/10.1126/science.1256014>
- Velez-Nicolas, M., García-López, S., Barbero, L., Ruiz-Ortiz, V., & Sánchez-Bellón, Á. (2021). Applications of unmanned aerial systems (UASs) in hydrology: A review. *Remote Sensing*, 13(7), 1359. <https://doi.org/10.3390/rs13071359>
- Ward, S. H., & Hohmann, G. W. (1988). 4. Electromagnetic theory for geophysical applications. In *Electromagnetic Methods in Applied Geophysics* (Vol. 1, Theory, edited, pp. 130–311). <https://doi.org/10.1190/1.9781560802631.ch4>
- Warren, C., Giannopoulos, A., & Giannakis, I. (2016). gprMax: Open source software to simulate electromagnetic wave propagation for Ground Penetrating Radar. *Computer Physics Communications*, 209, 163–170. <https://doi.org/10.1016/j.cpc.2016.08.020>
- Wilson, T. B., Kochendorfer, J., Diamond, H. J., Meyers, T. P., Hall, M., Lee, T. R., et al. (2024). Evaluation of soil water content and bulk electrical conductivity across the U.S. Climate Reference Network using two electromagnetic sensors. *Vadose Zone Journal*, 23(4), e20336. <https://doi.org/10.1002/vzj2.20336>
- Wu, K., & Lambot, S. (2022). Analysis of low-frequency drone-borne GPR for root-zone soil electrical conductivity characterization. *IEEE T GEOSCI REMOTE*, 60, 1–13. <https://doi.org/10.1109/tgrs.2022.3198431>
- Wu, K., Rodriguez, G. A., Zajc, M., Jacquemin, E., Clément, M., De Coster, A., & Lambot, S. (2019). A new drone-borne GPR for soil moisture mapping. *Remote Sensing of Environment*, 235, 111456. <https://doi.org/10.1016/j.rse.2019.111456>